Development and Characterisation of a Novel Light Detector: ArCLight

Masterarbeit der Philosophisch-naturwissenschaftlichen Fakultät
der Universität Bern

vorgelegt von
Livio Calivers

2021

Leiter der Arbeit:
Prof. Dr. Igor Kreslo

Abstract

Future neutrino experiments are focusing on precise measurements of the neutrino oscillation parameters. The discovery of a CP violation in the context of the neutrino oscillation would help to explain the matter-antimatter asymmetry in the universe. For higher sensitivity experiments novel detector technologies are required. The modular Liquid Argon Time Projection Chamber detector design developed by the ArgonCube collaboration addresses the challenges of the intense neutrino beams used in future long baseline experiments. The detector design is driven by the requirements for the Near Detector of the Deep Underground Neutrino Experiment. New compact light and charge readout technologies are needed to fit the modular structure. In this thesis, a novel dielectric light detection system, called ArCLight, is developed. Based on an existing concept, the performance of ArCLight is optimised through applying multiple design changes. In particular, the existing coating of a wavelength shifting material is replaced by a vacuum evaporation coating. The performance of ArCLight is characterised by measuring the Photon Detection Efficiency (PDE) and the spatial resolution. The new wavelength shifting coating has led to an increase of the overall PDE by about a factor two. The PDE of the final version was measured to be $(0.2055 \pm 0.0070)\,\%$.

Contents

List of Figures

List of Tables

Chapter 1

Introduction

Driven by experimental and theoretical findings in the 20th century, a theory describing the fundamental interactions in particle physics was developed. The so-called Standard Model (SM) unifies three of the four fundamental forces, namely the electromagnetic, weak and strong force. A vast number of experiments have shown results that are consistent with the SM predictions. However, i.a. the characterisation of the massive neutrally-charged neutrino and its interactions with matter do not agree with experimental measurements. In particular the discovery of neutrino oscillations is beyond the SM prediction of zero-mass neutrinos. Neutrino oscillations are caused by the non-consistency of neutrino flavour eigenstates and mass eigenstates and could potentially evoke a Charge Parity symmetry (CP) violation which could help to explain the matter-antimatter asymmetry in the universe.

The parameters of neutrino oscillations have been studied in several experiments over the last 25 years as they can not be deduced theoretically. Due to the low cross-section of neutrino interactions and the consequently low statistics these measurements are limited by high uncertainties. In particular, the existence of CP violation due to neutrino mixing remains unresolved. Also, the determination of the neutrino mass or the ordering of the mass eigenstates is as yet unknown. Current experiments do not have a high enough sensitivity to solve the neutrino mass ordering problem.

To resolve these problems, new experiments with higher sensitivities are planned. In the past neutrinos originating from the sun, the atmosphere or nuclear reactors were studied. In order to get more statistics artificial neutrino beams with high intensities are needed. These are achieved by firing high energy proton beams into fixed targets and magnetically focusing the produced pions. The pions decay to neutrinos forming a relatively intense beam. Despite the high beam intensity, large mass detectors are demanded to get high enough interaction rates. One of the most promising detector type enabling high mass but enabling a relatively compact detector designs is the Liquid Argon (LAr) Time Projection Chamber (TPC). But existing LAr TPCs are not applicable in challenging environments with the high-multiplicity environments in intense neutrino beams. Novel LAr TPC technologies are required to attack those challenges. An approach to implement a large scale LAr TPC fulfilling these requirements is the ArgonCube concept. The ArgonCube collaboration is developing a modular detector design involving new charge and light readout technologies.

The ArgonCube design will be applied in the Near Detector (ND) of the Deep Under-

ground Neutrino Experiment (DUNE). DUNE is a planned long-baseline experiment using an aforementioned proton-induced neutrino beam. Experiments with a long baseline between an ND and a Far Detector (FD) can be optimised to achieve a high sensitivity on certain oscillation parameters. With a baseline length of 1300 km, DUNE aims to improve the current measurements on the CP violation parameter and solving the mass ordering problem. To achieve a high sensitivity, LAr TPCs are used for both the ND and the FD which minimises cross section uncertainties between the two. LAr TPCs commonly used Photo Multiplier Tubes (PMTs), but these are not applicable in the ArgonCube design as they would occupy too large a volume. In ArgonCube two complementary dielectric light detection systems are implemented. These are the Light Collection Module (LCM) developed by the Joint Institute for Nuclear Research (JINR) which shows a high Photon Detection Efficiency (PDE) and the Argon Cube Light detector (ArCLight) developed by the Laboratory for High Energy Physics (LHEP) in Bern. The latter has a more limited PDE, but therefore is designed to provide a higher spatial resolution and larger dynamic range.

In this thesis, ArCLight is developed based on an existing prototype design. ArCLight is a compact dielectric light trap with a large sensitive area read out by Silicon Photo Multipliers (SiPMs). The goal is to have a design fulfilling the requirements for the DUNE ND. These requirements are particularly driven by the demands for an efficient tagging of fast neutrons produced in neutrino interactions. This tagging can only be achieved by the light detection system as it requires a fast timing which is not provided by the charge readout. Furthermore, a good spatial resolution and a high enough PDE is needed, in order to provide $T0$ for neutrino events and to tag beam related background.

In Chapter 2 the history and the current status of neutrino oscillation physics is outlined. Also, an outlook to future experiments, in particular the DUNE experiment, is given. The working principle and properties of LAr TPCs are elucidated in Chapter 3. In Chapter 4 the detector concept developed by the ArgonCube collaboration is discussed in detail. Here, also the planing of the prototyping campaign for the DUNE ND is presented, which this thesis is part of. Also discussed are the requirements on the light and charge readout as motivated by the DUNE ND physics requirements. In course of this thesis, I adapted the existing ArCLight design and optimised the production procedure. The design changes are discussed in detail in Chapter 5. The whole characterisation of the ArCLight detector is discussed in Chapter 6. I studied the impact of the design changes on the PDE in a GEANT4 based optical simulation and as-well as in multiple experiment test runs. This simulation was originally implemented by Francesco Piastra and Patrick Koller and was optimised and adapted within this work. These tests were part of the prototyping plan in which also other detector parts and the fully integrated system were tested. By using the output of the optical simulation, I could establish an algorithm to reconstruct the coordinates of the light emission point. I then applied, this algorithm to the experimental data to get a first estimation of the spatial resolution of ArCLight. The measured PDE of the final ArClight version is used to establish an energy threshold for the detection of charged particles. Using an existing simulation study, this threshold can be compared with the energy spectrum of neutron-induced recoil particles for the DUNE ND. The original plots and simulations used in this section were generated by Patrick Koller. In the last chapter the insights of this thesis are concluded and an outlook for the next steps is given.

Chapter 2

History of Neutrino Research

In this chapter, the history of neutrino physics, in particular neutrino oscillation physics, is outlined. The first section covers the major breakthroughs in experimental neutrino physics. As this thesis is focusing on the detector design for future neutrino oscillation experiments, the oscillation theory and its main consequences are summarized in Section 2.2. The last part of this chapter discusses future neutrino oscillation experiments. In particular, the DUNE experiment is introduced.

2.1 History of neutrino experiments

In the early 20th century, the physics world was puzzled by multiple experiments measuring the continual energy spectrum of electrons emitted by β-decays. As the β-decay was considered to be a two-body decay (electron and daughter nucleus), one would expect a discrete energy of the emitted electron. This however was proven not to be the case in 1914 by James Chadwick [1]. To address this, in his famous letter in 1930, Wolfgang Pauli proposed a neutral charged spin 1/2 particle with a mass "lower than 0.01 proton masses" [2], which Pauli called "neutron". Redefining the β-decay to the emission of an electron and a "neutron" explained the measured continuous spectrum. In 1932 Chadwick discovered the neutron [3]. However, Francis Perrin deduced that the mass of the particle emitted in the β-decay has to be of mass significantly lower than the electron mass and thus could not be the particle discovered by Chadwick. Pauli's particle was renamed the "neutrino" by Enrico Fermi who came up with a theory explaining the β-decay [4]. Using Fermi's theory, Hans Bethe and Rudolph Peierls showed that the neutrino-nucleus cross section must be $< 10^{-44}\mathrm{cm}^2$, and concluded "that there is no practically possible way of observing the neutrino" [5].
It took 26 years between the proposal and the first detection of the neutrino. In 1956, Clyde Cowan and Frederick Reines published results from their inverse β-decay experiment where they detected the first electron antineutrinos [6]. In an inverse β-decay an electron antineutrino interacts via

$$\overline{\nu}_\mathrm{e} + \mathrm{p} \rightarrow \mathrm{n} + \mathrm{e}^+. \tag{2.1}$$

Cowan and Reines placed a water target next to the Savannah River nuclear reactor in South Carolina (USA) to have a high neutrino flux. The positron emitted in the inverse

β-decay interacts with shell electrons producing two back-to-back photons. By doping the water with cadmium, which captures free neutrons, one gets further photon emission. The neutron-induced scintillation light occurs a few µs later. Thus, measuring two light pulses shortly after each other is a distinct signal for a $\overline{\nu}_{\mathrm{e}}$ with very low background. However, the experiment of Reines and Cowan was limited to the detection of $\overline{\nu}_{\mathrm{e}}$.
One year later, based on the experiments of Chien-Shiung Wu and Maurice Goldhaber it could be ascertained that only left-handed neutrinos (and right-handed anti-neutrinos) can interact via weak coupling [7]. The experiment was also the first to demonstrate parity-symmetry (P) violation by the weak interaction.
In 1962, a group led by Leon M. Ledermann discovered the ν_{μ} [8]. This experiment was the first to use neutrinos produced by an accelerator beam. By shooting protons on a beryllium target pions are produced, these pions decay as:

$$\pi^{+} \rightarrow \mu^{+} + \nu_{\mu}, \tag{2.2}$$

$$\pi^{-} \rightarrow \mu^{-} + \overline{\nu}_{\mu}, \tag{2.3}$$

emitting a ν_{μ} (or a $\overline{\nu}_{\mu}$). By applying a magnetic field right after the target μ^{+} can be focused and μ^{-} defocused, or vice versa. After blocking the $\pi^{\pm}$ with an iron shield one gets a pure ν_{μ} (or $\overline{\nu}_{\mu}$) beam. In the Ledermann experiment, a spark chamber was used to detect charged particles from interacting neutrinos. In a spark chamber charged particles ionise a gas and this ionisation is made visible by applying a high voltage between several metal plates placed in the chamber.
In 1967, Andrei Sakharov set out the requirements to explain the matter-antimatter asymmetry in the universe through baryon-generating interactions [9]. The following three so-called "Sakharov conditions"

- baryon number violation
- charge-symmetry (C) and charge-parity-symmetry (CP) violation
- interactions out of thermal equilibrium

must be fulfilled for a given interaction in order to produce matter and antimatter at different rates. The first two conditions ensure that more baryons than anti-baryons are produced. The third condition is needed since else charge-parity-time (CPT) symmetry would allow the inverse process annihilating the net baryon - anti-baryon difference. Processes fulfilling these conditions could be observed i.a. in the quark sector but the CP violation has been too low to explain the observed matter-antimatter asymmetry [10]. Thus, further CP violating processes have to be discovered to explain the full asymmetry.
In 1968, Raymond Davis, Don S. Harmer and Kenneth C. Hoffman measured solar neutrinos for the first time in the Homestake Mine, South Dakota (USA) [11]. Solar neutrinos are produced by fusion reactions taking place in the sun. However, the measured neutrino flux was only two-thirds of the expected flux calculated by solar models [12]. This discrepancy became known as the solar neutrino problem [13, 14]. The Homestake experiment was based on the interaction of ν_{e} with ^{37}Cl dissolved in water via

$$\nu_{\mathrm{e}} + {}^{37}\mathrm{Cl} \rightarrow \mathrm{e}^{-} + {}^{37}\mathrm{Ar}. \tag{2.4}$$

The number of neutrino interactions in this experiment could only be determined offline by measuring the activity of the radioactive ^{37}Ar content. The experiment was located $\sim 1500\,\mathrm{m}$ below to prevent cosmic radiation background.
The solar neutrino problem can be explained by neutrino oscillations. The theory was purposed by Bruno Pontecorvo in 1968 [15]. It purposes that neutrinos can transform into a different neutrino species during the evolution in time and space.
In 1975 the τ lepton was discovered by Martin L. Perl [16] which directly implied the proposal of a third neutrino flavour ν_τ [17].
A similar result as the solar neutrino problem was found for atmospheric neutrinos by the Kamiokande-II experiment in 1988 [18] and later in 1991 in the Irvine–Michigan–Brookhaven (IMB) experiment [19]. Both experiments were mainly sensitive for atmospheric neutrinos but also solar neutrinos could be measured. Atmospheric neutrinos are produced via decaying pions occurring in the Earth's atmosphere. The pions are produced by cosmic protons interacting with nuclei in the atmosphere. The Kamiokande experiments (Kamiokande I and II, Super-Kamiokande) is a series of experiments with water Cherenkov detectors located in the Mozumi Mine in Japan. IMB was also a water Cherenkov detector which was located in a mine in Fairport Harbor, Ohio (USA). A particles passing through the ultra-pure water of the detectors, has a speed that exceeds the speed of light in water, this produces an observable cone-shaped light emission along the particles trajectory; the so-called Cherenkov light [20]. This characteristically blue light is detected by Photo Multiplier Tubes (PMTs). By reconstructing the opening angle of the Cherenkov cone, the momentum and direction of the particle can be deduced. This detector type is sensitive for both ν_e and ν_μ, as-well as $\overline{\nu}_\mathrm{e}$ and $\overline{\nu}_\mu$, via the Charged Current (CC) interactions, i.a. the Quasi-Elastic (QE) interaction

$$\nu_\ell + \mathrm{n} \rightarrow \ell^- + \mathrm{p}, \tag{2.5}$$

$$\bar{\nu}_\ell + \mathrm{p} \rightarrow \ell^+ + \mathrm{n}, \tag{2.6}$$

and the electron scattering

$$\nu_\mathrm{e} + \mathrm{e}^- \rightarrow \nu_\mathrm{e} + \mathrm{e}^-. \tag{2.7}$$

Due to the low energy of solar and atmospheric neutrinos ν_τ and $\overline{\nu}_\tau$ interactions are not observable via CC interactions as the energy required to produce a $\tau^\mp$ is too high. The electron scattering via CC is only viable for ν_e. Both IMB and the Kamiokande experiments were not sensitive to Neutral Current (NC) interactions and thus could not measure the total neutrino flux.
In 1990, at the Large Electron-Positron Collider (LEP) in Geneva (Switzerland) precise measurements of the Z^0 boson were conducted. With the cross section obtained in these measurements, the number of light neutrino coupling by weak interaction could be deduced to be three [21]. This consolidated the proposal of the ν_τ and ruled out the existence of further weak-interacting light neutrinos.
In the latest operating version of the Kamiokande experiments, the 50 kt Super-Kamiokande, the atmospheric neutrino problem was further studied. In 1998, it was measured that the ν_μ flux is $\approx 50\,\%$ lower for upwards directed atmospheric neutrinos which pass through the earth before hitting the detector than neutrinos originated in the atmosphere directly above the detector [22]. However, since the total neutrino flux could not be measured it was unclear if the missing neutrinos were actually disappearing.

The previously proposed ν_τ was first detected in 2001 at the Direct Observation of the Nu Tau (DONUT) experiment at Fermilab [23]. A 800 GeV proton beam was used to produce the charmed meson D_s, similar to the Ledermann experiment, which decays to a $\overline{\nu}_\tau$ and a τ^-. In an emulsion detector, the τ could be detected that was produced by a charged current ν_τ interaction.
The existence of neutrino oscillation was experimentally confirmed in 2002 by the Sudbury Neutrino Observatory (SNO) experiment in Ontario (Canada) [24]. The 1 kt water Cherenkov detector was filled with heavy water (D_2O), which enabled the detection NC interactions in addition to CC interactions.

$$\nu_\ell + \mathrm{d} \rightarrow \nu_\ell + \mathrm{n} + \mathrm{p}, \tag{2.8}$$

$$\bar{\nu}_\ell + \mathrm{d} \rightarrow \bar{\nu}_\ell + \mathrm{n} + \mathrm{p}, \tag{2.9}$$

where ℓ =e,μ,τ. A method to detect the emitted neutrons in this interaction channel allowed to determine the total neutrino flux. The total flux was measured to be consistent with the model expectations as expected by the neutrino oscillation theory. The discovery of neutrino oscillation directly implied a non-zero neutrino mass (see justification in the next section).
Since its discovery, the properties of neutrino oscillations have been studied by various experiments. In particular, the Daya Bay Reactor Neutrino Experiment in 2012 [25] and Tokai To Kamioka (T2K) in 2013 [26]. The Daya Bay experiment studies neutrinos originated from several reactors located around the grid of eight liquid scintillator detectors located at Daya Bay (China). The T2K experiment is a long baseline experiment which sends a neutrino beam over from the J-PARC facility in Tokai (Japan) to the Super-Kamiokande detector which is 295 km from Tokai. In a close distance to the beam origin, a second detector complex is placed to the initial neutrino flux. Both Day Bay and T2K reported the mixing angle θ_{13} to be well above zero. A non-zero θ_{13} allows for CP violation in neutrino oscillation, as will be shown in the next section. The combined findings on the full set of oscillation parameters are elucidated in the next section.

2.2 Neutrino oscillation

In this section, the theory and the current state of research in neutrino oscillation physics is summarised following Bettini [27] if not otherwise specified. The theory of neutrino oscillation is based on the non-equality of neutrino flavour eigenstates (ν_e,ν_μ,ν_τ) and neutrino mass eigenstates (ν_1,ν_2,ν_3). Note, there is no argument restricting the number of mass eigenstates to three. However, any further state would not be active in weak interactions and therefore is not further discussed in the following. The two sets of eigenstates are connected via a unitary mixing matrix, called the Pontecorvo-Maki-Nakagawa-Sakata (PMNS) matrix [28], as

$$\begin{pmatrix} \nu_e \\ \nu_\mu \\ \nu_\tau \end{pmatrix} = U_{PMNS} \cdot \begin{pmatrix} \nu_1 \\ \nu_2 \\ \nu_3 \end{pmatrix}. \tag{2.10}$$

The PMNS matrix is historically split up into rotations around the three angles θ_{23},θ_{13} and θ_{12}. Further one can introduce a CP-violating phase δ_{CP} without breaking the unitarity of the matrix. A non-zero (and non-π) value for δ_{cp} (and $\theta_{13} \neq 0$) implies a CP violation

due to the neutrino oscillation mechanism. Motivated by the suppression of the neutrino mass, if one allows the neutrino to be a Majorana fermion ($\nu = \bar{\nu}$) two additional phases Φ_1 and Φ_2 have to be added. Splitting the PMNS matrix up to the different rotation matrices (plus one for the Majorana phases) one gets

$$U_{PMNS} = \begin{pmatrix} 1 & 0 & 0 \\ 0 & c_{23} & s_{23} \\ 0 & -s_{23} & c_{23} \end{pmatrix} \begin{pmatrix} c_{13} & 0 & s_{13}e^{-i\delta} \\ 0 & 1 & 0 \\ -s_{13}e^{-i\delta} & 0 & c_{13} \end{pmatrix} \begin{pmatrix} c_{12} & s_{12} & 0 \\ -s_{12} & c_{12} & 0 \\ 0 & 0 & 1 \end{pmatrix} \begin{pmatrix} 1 & 0 & 0 \\ 0 & e^{i\Phi_1} & 0 \\ 0 & 0 & e^{i\Phi_2} \end{pmatrix}, \tag{2.11}$$

where $c_{ij} = \cos\theta_{ij}$ and $s_{ij} = \sin\theta_{ij}$. This splitting has a historical background as the single matrices represent the mixing observable in either solar, reactor and atmospheric neutrino experiments, respectively. For the discussion of oscillation probabilities the Majorana phases cancel and can therefore have no effect.
Considering the momentum of neutrinos originating from the same source to be p, one can use the ultra-relativistic approximation of the energy of a neutrino in mass eigenstate i as

$$E_i = \sqrt{p^2 + m_i^2} \approx p + \frac{m_i^2}{2p} \approx p + \frac{m_i^2}{2E}, \tag{2.12}$$

where E is the average energy of the different states. The evolution of a single state in time can be described by the plane wave approximation as

$$|\nu_i(t)\rangle = e^{-iE_i t} |\nu_i(0)\rangle . \tag{2.13}$$

As the different mass eigenstates have different E_i, their evolution in time differs, which leads to differences in the observable flavour state compared to $t = 0$.
When propagating in a vacuum, the probability that a neutrino of flavour state α is transferred to state β after a time t is

$$\begin{aligned} P(\nu_\alpha \to \nu_\beta) =& \left|\left\langle \nu_\beta \middle| \nu_\alpha(t) \right\rangle\right|^2 \\ =& \left| \sum_j \sum_i U_{\beta j} U^*_{\alpha i} e^{-iE_i t} \left\langle \nu_j \middle| \nu_j \right\rangle \right|^2 \\ =& \delta_{\alpha\beta} - 4 \sum_{i<j} \mathrm{Re}\left[U_{\alpha i} U^*_{\beta i} U^*_{\alpha j} U_{\beta j}\right] \sin^2\left(\Delta m^2_{ij} \frac{L}{4E}\right) \\ &+ 2 \sum_{i<j} \mathrm{Im}\left[U_{\alpha i} U^*_{\beta i} U^*_{\alpha j} U_{\beta j}\right] \sin\left(\Delta m^2_{ij} \frac{L}{2E}\right), \end{aligned} \tag{2.14}$$

where $L \approx ct$ is the distance travelled by the neutrino and Δm_{ij} is the absolute mass difference between the mass states i and j [29]. Neutrino oscillation can only occur when $\Delta m_{ij} \neq 0$. Therefore, measuring neutrino oscillations intrinsically proved that neutrinos have non-zero mass. By tuning the $\frac{L}{E}$ ratio for a experiment, the appearance or disappearance effect of single neutrino flavours can be optimised to measure in a range with a high sensitivity for the single parameters.
Eq. 2.14 is only valid for oscillations in vacuum; for neutrinos travelling through matter interactions with shell electrons have to be considered. This so-called Mikheyev-Smirnov-Wolfenstein (MSW) effect mainly affects ν_e and $\overline{\nu}_\mathrm{e}$ and thus differs for the various mass eigenstates [30]. The MSW effect enables to study the masses of the different eigenstates

Table 2.1 – Global fit on the three-flavour neutrino oscillation parameter (NuFit 5.0). All data obtained from various experiments until July 2020 except the latest Super-Kamiokande atmospheric data. [31]

Parameter	Normal ordering ($\pm 1\sigma$)	Inverted ordering ($\pm 1\sigma$)
θ_{12} [°]	$33.44^{+0.78}_{-0.75}$	$33.44^{+0.78}_{-0.75}$
θ_{13} [°]	$8.57^{+0.13}_{-0.12}$	$8.61^{+0.12}_{-0.12}$
θ_{23} [°]	$49.0^{+1.1}_{-1.4}$	$49.3^{+1.0}_{-1.2}$
δ_{CP} [°]	195^{+51}_{-25}	286^{+27}_{-32}
Δm^2_{21} [eV^2]	$7.42^{+0.21}_{-0.20} \cdot 10^{-5}$	$7.42^{+0.21}_{-0.20} \cdot 10^{-5}$
Δm^2_{31} [eV^2]	$2.514^{+0.028}_{-0.027} \cdot 10^{-3}$	$2.514^{+0.028}_{-0.028} \cdot 10^{-3}$

in long baseline experiments with suitable parameters. However, up until today, no experiment had a high enough sensitivity to determine the ordering of the masses. There are two potential scenarios, the normal ($m_1 < m_2 < m_3$) and the inverted ($m_3 < m_1 < m_2$) ordering.
The results of the latest global fit (NuFit 5.0) are shown in Tab. 2.1. So far normal ordering is favoured at the 1.6σ level but not confirmed [31]. For normal mass ordering, $\delta_{CP} = \pi$ is within a 0.6σ interval of the fit, which would imply that there is no CP violation due to neutrino oscillation. For the inverted mass ordering a non-CP violating phase can be excluded at a 3σ level.

2.3 Next generation experiments

As shown in the previous section, the uncertainties on some of the neutrino oscillation parameters are still huge. In particular, the main questions if there is a CP violation in neutrino oscillations and the mass ordering are so far unsolved. The Next generation experiments with increased sensitivity are vital to answer those questions. To optimise and control the parameters especially L and E to a high degree of accuracy, long baseline experiments with accelerator neutrino beams are the optimal choice. They can be optimised for measuring exactly these parameters. To fit the requirements for higher sensitivity two large scale experiments with two different approaches are planed.
One these experiments is Hyper-Kamiokande [32]. It is another part of the existing Kamiokande experiment series in Japan. The Hyper-Kamiokande has the nearly identical detector design as the Super-Kamiokande but 20 times larger mass. The corresponding Tokai-to-Hyper-Kamiokande (T2HK) is an upgrade of the existing long baseline experiment T2K. T2HK, like its predecessor T2K, uses an accelerator neutrino beam originated at the J-PARC facility in Tokai. An ND located close to the beam origin will analyse the beam that is then sent to the Hyper-Kamiokande detector.
The other experiment is DUNE [34–36]. The DUNE collaboration plans to use the existing accelerator facilities at the Fermi National Accelerator Laboratory (Fermilab) to produce $\nu_\mu/\overline{\nu}_\mu$ beam with a maximum power of 1.2 MW (2.4 MW for phase II). The

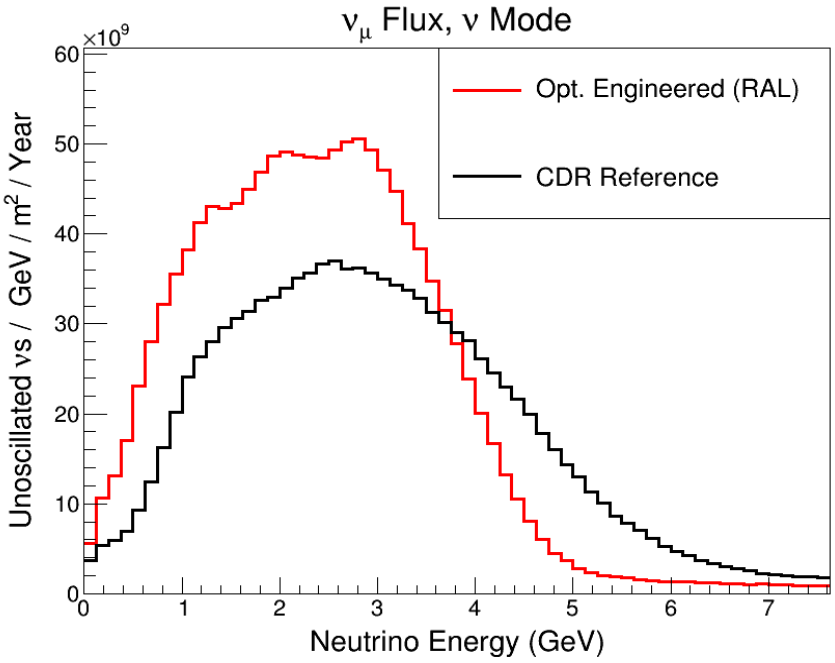

Figure 2.1 – Expected beam profile for the DUNE experiment as stated in the CDR (red) and a further optimised version (black). The maximum flux is expected at a neutrino energy of $\approx 3\,\text{GeV}$. [33]

experimental parameters, in particular $\frac{L}{E}$, are optimised to have a high sensitivity to δ_{CP}. The expected beam profile is depicted in Fig. 2.1. Further, it is optimised to investigate the neutrino mass ordering via the MSW effect. In Fig. 2.2 the expected sensitivity for both CP violation and mass ordering are depicted. After a seven years exposure, only a strong CP violation ($\delta_{CP} \sim \pm\frac{\pi}{2}$) could be confirmed at the 5σ level but for a relatively broad range. The mass ordering is expected to be deduced at the 5σ level for any δ_{CP} value after seven years of exposure.

The DUNE FD will be placed in the Sanford Underground Research Facility (SURF), South Dakota (USA) at a 1300 km distance to the beam origin. It consists of four Liquid Argon Time Projection Chambers (LArTPC) detectors and has a total active mass of 40 kt, the event rate in the FD will be 3.4 beam neutrinos per hour. The interaction rate measured at the far detector is

$$\left.\frac{\mathrm{d}N(\nu_\alpha)}{\mathrm{d}t}\right|_{FD} = \Phi_{FD}\sigma_{FD}\epsilon_{FD}P(\nu_\mu \to \nu_\alpha), \tag{2.15}$$

where Φ is the ν_μ flux, σ_{FD} the neutrino cross section in the FD and ϵ_{FD} the efficiency of the FD.

A ND placed close to the beam origin measures the interaction rate

$$\left.\frac{\mathrm{d}N(\nu_\beta)}{\mathrm{d}t}\right|_{ND} = \Phi_{ND}\sigma_{ND}\epsilon_{ND}. \tag{2.16}$$

By choosing the same detector type for the ND and FD the cross section is the same for both. Thus by taking the ratio of the two interaction rates the systematic uncertainty in the measurement of the oscillation probability can be significantly decreased.

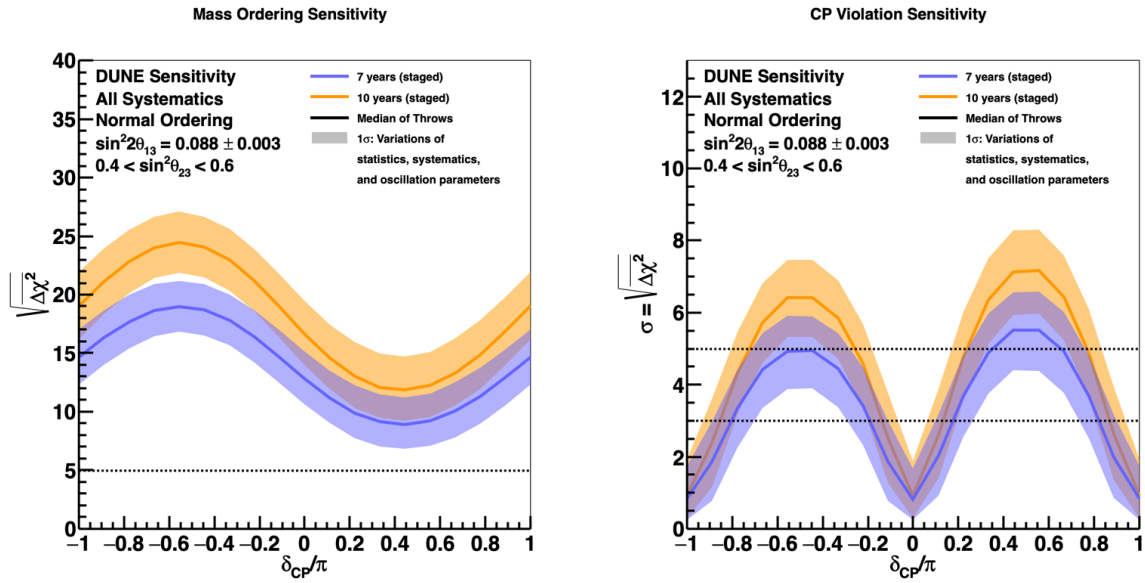

(a) (b)

Figure 2.2 – Expected sensitivity of the DUNE experiment on (a) CP violation ($\delta_{CP} \neq 0, \pi$) (b) mass ordering as a function of true δ_{CP} assuming normal mass ordering. The equivalent plots assuming inverted mass ordering show similar results and are therefore not depicted. [37]

The ND will be placed 574 m from the beam target in a cavern $\sim$ 60 m underground. It will be built up of three sub-detectors: a LArTPC detector (ND-LAr), a muon spectrometer and a beam monitor. ND-LAr will have a mass of 147 t and see 29.4 beam neutrinos every 10 µs beam spill. ND-LAr and the spectrometer are placed on a movable support structure enabling off-axis measurements with a narrower neutrino energy spectrum, while the beam monitor stays on axis.
LArTPCs are the subject of this work; their development for their application to the DUNE ND will be discussed in the coming chapters.

Chapter 3

Liquid Argon Time Projection Chambers

LAr TPCs are being employed to meet the requirements of future neutrino experiments as they provide a high density target that combines precise tracking and calorimetry. In this chapter, the working principle of a LAr TPCs is described. Furthermore, the requirements on charge and light readout in LAr TPCs are elucidated.

3.1 Detection principle

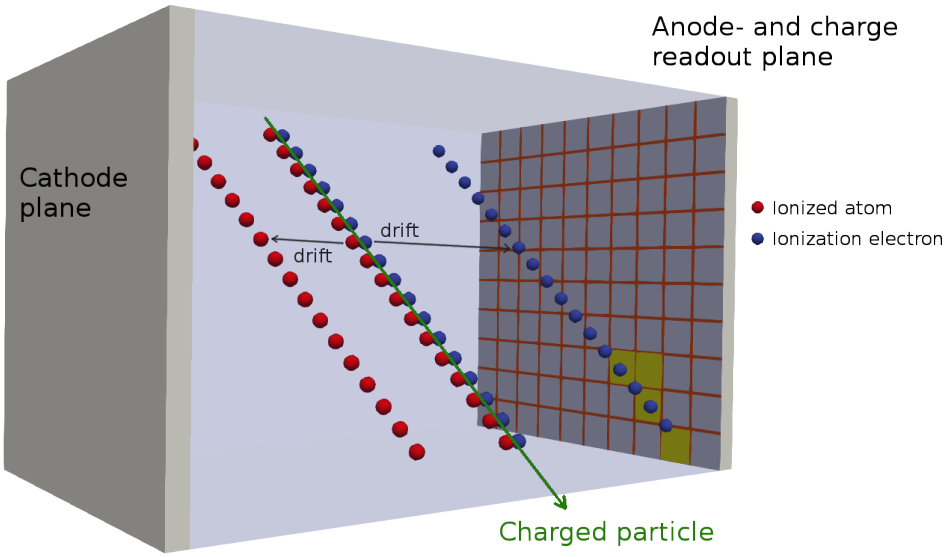

Figure 3.1 – Scheme of the LAr TPC detection principle. A charge particle crossing the detector (green) leaves a track of ionised atoms (red) and free electrons (blue). The electrons drift towards the anode- and charge readout plane and get detected. Here, a pixelated charge readout is illustrated. [38]

A Time Projection Chamber is a 3D tracking detector based on a noble gas or liquid as the sensitive medium developed by David Nygren in 1974 [39]. A TPC consists of

a cathode plane that is held on a negative electrical potential and a charge readout plane at zero potential. The TPC structure is submerged in the sensitive medium. A schematic depicted in Fig. 3.1 illustrates the detection principle. When a charged particle crosses the active volume it leaves a track of ionised atoms and ionisation electrons. By applying an electric field between cathode and anode, the ionised atoms and ionisation electrons drift in opposite directions. In order to prevent the ion-electron pair from recombining instantly, a field strength of $\mathcal{O}\left(500\,\mathrm{V\,cm^{-1}}\right)$ is needed. If the lifetime of a free electron in the sensitive medium is long enough, the electrons can drift all the way to the charge readout plane. Therefore, only noble gases or liquids can be applied as the sensitive medium since only those can provide a long electron lifetime due to their low electronegativity. The timing information of the charge arriving at the readout plane enables a projection into three dimensional information of the collected charge. However, by measuring only the collected charge, the absolute position in the drift direction of the charged particle interaction is unknown. This issue can be solved by also measuring prompt scintillation light that occurring within $\mathcal{O}$(ns) after the interaction. The obtained timestamp, T_0, of the scintillation light can be used to set the coordinate position of the interaction within the TPC volume.

3.2 Liquid argon as detection medium

In 1974 Willisam J. Willis and Veljko Radeka started using LAr in ionisation chambers. Three years later Carlo Rubbia applied Willis and Radekas technique to the original TPC design of Nygren, proposing the LAr TPC as a neutrino detector [40]. LAr has excellent properties for the application in TPCs, a passing particle leaves a large amount of ionisation charge and scintillation light at the same time. A list of the main properties relevant for the application in a TPC are given in Tab. 3.1. LAr has a high density of $1399\,\mathrm{kg\,m^{-3}}$ which helps to overcome aforementioned low neutrino cross section. The presence of argon in earth's atmosphere (0.93 % [41]) and the fact that it is widely used in industry makes it cheaply available in large amounts and thus applicable for large scale detectors (compared to xenon). LAr has a temperature of $\sim 87\,\mathrm{K}$ (at atmospheric pressure) which requires a cryogenic detector setup with proper isolation and cooling.
In order to enable an accurate charge readout, the ionisation and charge transport properties are crucial.
The energy loss of an incoming particle due to ionisation is described by the Bethe-Bloch formula as

$$-\left\langle \frac{dE}{dx} \right\rangle = K z^2 \frac{Z}{A} \frac{1}{\beta^2} \left[\frac{1}{2} \mathrm{Ln} \left(\frac{2 m_e c^2 \beta^2 \gamma^2 W_i}{I_0^2} \right) - \beta^2 - \frac{\delta}{2} \right], \tag{3.1}$$

where $K = 0.307\,\mathrm{MeV\,mol^{-1}\,cm^2}$, Z and A the atomic number and atomic mass of the atoms in the medium respectively, β and γ the relativistic factors of the incoming particle,m_e the electron mass, I_0 the mean excitation potential, δ a density correction (because of polarisation in medium) and W_i the energy needed per electron-ion pairs. From the formula, it follows that a minimum in the energy loss due to ionisation exists. For LAr this minumum is $2.1\,\mathrm{MeV\,cm^{-1}}$, a particle having this characteristic energy loss is called a Minimum Ionising Particle (MIP). In LAr crossing cosmic muons can be approximated as MIPs with a high accuracy. The number of produced electron-ion pairs

Symbol	Property	Value
ρ_{BP}	Density (@ boiling point)	1399×10^3 kg [42]
T_B	Boiling point (@ 1 bar)	87.30 K [42]
X_0	Radiation length	14.0 cm [43]
dE/dx	Ionisation energy loss per distance	2.1 MeV cm^{-1} [43]
W_i	Required energy per electron-ion pair	23.6 eV [44, 45]
μ	Electron mobility (@ E=500 V cm^{-1})	329.66 cm^2/Vs [46–49]
v	Electron drift velocity (@ E=500 V cm^{-1})	0.165 cm µs^{-1} [46–49]
λ	Scintillation emission wavelength	128 nm [50]
$W_{ph,max}$	Required energy per photon for a MIP (@E=0)	24.4 eV [51]
L_R	Rayleigh scattering length	55 cm to 95 cm† [52–55]
D_L	Longitudinal diffusion coefficient	6.82 cm^2/s [56, 57]
D_T	Transverse diffusion coefficient	13.16 cm^2/s [56, 58]

Table 3.1 – List of liquid argon properties. †The measured Rayleigh scattering length varies greatly between the values obtained in ProtoDUNE and measurements done in dark matter experiments. Thus not a single value can be stated here.

is limited by W_i. Since the charge readout only records the number of produced electrons, W_i is a limiting factor for the energy resolution of the detector.
Due to recombination of produced electron-ion pairs, the full produced charge does not arrives at the readout plane. The amount of charge that can be collected is described by the box model as

$$Q = Q_0 \cdot \frac{Ln(1+\xi)}{\xi}, \tag{3.2}$$

where Q_0 is the initially produced charge by ionisation and ξ is a field-dependent parameter proportional to E^{-1} [59]. Thus, with a higher drift field more charge can be collected. Furthermore, the fraction of charge that arrives at the readout plane gets reduced by impurities as free electrons can get attached to impurities. Impurities with high electronegativity can reduce the mean electron lifetime in LAr drastically, in the worst case no tracks are observable. The velocity of a electron in an electric field is $v = E \cdot \mu$, where μ is the electron mobility. For $E = 500\,\mathrm{V\,cm^{-1}}$ and a maximum drift length of 50 cm, the maximum drift time of an electron is 303 µs. Within this time the electrons also move in transverse direction to the drift direction due to diffusion. Also in drift direction diffusion causes a smearing in the electron velocity and thus a coordinate smearing. Depending upon its magnitude, diffusion can limit or enhance the spatial resolution of the charge readout. The smearing due to diffusion for a drift time t is

$$\sigma_{L/T} = \sqrt{2 D_{L/T} t}, \tag{3.3}$$

where $D_{L/T}$ is the the longitudinal or transversal diffusion coefficient, respectively [60]. Thus, at the same field strength shorter drift lengths reduce the effect of diffusion.
The scintillation process in liquid argon emits light at a single peak around 128 nm. The photon emission is induced by the decay of the singlet or triplet state of an excited dimer. Thus, also two decay time constants are observable, a fast time component in $\mathcal{O}(5\,\mathrm{ns})$ and a slow component in $\mathcal{O}(1.5\,\mu\mathrm{s})$ [61]. These excited dimer states can be induced by

directly excited atoms A^*

$$\begin{aligned} A^* + A + A &\rightarrow A_2^* + A, \\ A_2^* &\rightarrow 2A + h\nu, \end{aligned} \tag{3.4}$$

or by recombination of ionised atoms A^+

$$\begin{aligned} A^+ + A &\rightarrow A_2^+, \\ A_2^+ + e^- &\rightarrow A^{**} + A, \\ A^{**} &\rightarrow A^* + \text{heat}, \\ A^* + A + A &\rightarrow A_2^* + A, \\ A_2^* &\rightarrow 2A + h\nu, \end{aligned} \tag{3.5}$$

where $h\nu$ represents a emitted VUV photon and heat denotes the de-excitation by heat emission [51]. Singlet and triplet states can be be formed through both of the processes [62]. Due to the low binding energy of A_2 of 12.3 meV a not negligible fraction of the Argon atoms is permanently in a dimer state, which could lead to a reabsorbtion of the scintillation light [63]. However, the binding energy of the A_2^* state is significantly stronger than of the one of A_2. This leads to a massive Stokes' shift and thus reabsorbtion hardly ever occurs.

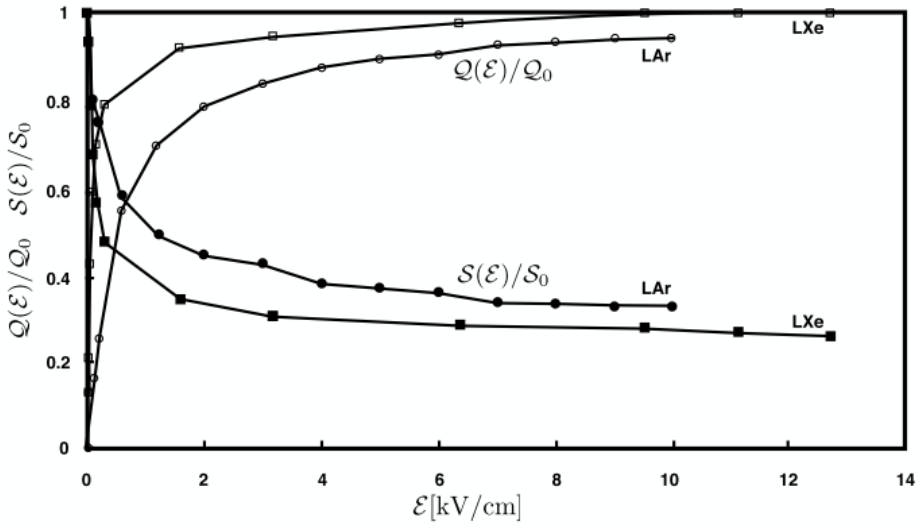

Figure 3.2 – Ionisation (non-filled symbols) and scintillation yield (filled symbols) in LAr and liquid xenon (LXe). $S(E)/S_0$ is the relative light yield to zero-field conditions and $Q(E)/Q0$ is the relative ionisation yield compared to infinite-field conditions.[51]

As the scintillation process can be induced by recombination (Eq. 3.5), any process reducing the recombination rate reduces the light yield. Thus, applying an electric field reduces the number of photons that can be collected at the light detectors [51]. At the same time the amount of collected charge increases. This anti-correlation is shown in Fig. 3.2

3.3 Requirements on charge and light detectors

The working principle of TPCs and the properties of LAr as a sensitive medium put certain requirements on the charge and light readout. These requirements, however, are also mainly driven by the sensitivity or resolution that has the be reached in a certain experiment. For DUNE, these requirements and how to fulfil them are extensively discussed in the next chapter. Here, the general requirements driven by the working principle of LAr TPCs and commonly used readout techniques are discussed.
The charge readout of a LAr TPC needs to be able to measure low amounts of charge with a good spatial resolution. Considering a MIP passing the detector, following Eq. 3.2, the amount of collectable charge per track length can be calculated as

$$\frac{\mathrm{d}Q}{\mathrm{d}x} = \frac{\mathrm{d}E/\mathrm{d}x_{MIP}}{W_i}\frac{Ln(1+\xi)}{\xi}e \tag{3.6}$$

$$\approx \frac{2.1\,\mathrm{MeV\,cm^{-1}}}{23.6\,\mathrm{eV}}\frac{Ln(1+1.6)}{1.6}e \tag{3.7}$$

$$\approx 5310\,e\,\mathrm{mm^{-1}} \tag{3.8}$$

$$\approx 0.85\,\mathrm{fC\,mm^{-1}}, \tag{3.9}$$

where $\xi = 1.6$ was approximated for a $E = 500\,\mathrm{V\,cm^{-1}}$ drift field. Especially for large detectors, this brings major challenges as one needs a large number of channels with a relatively high charge sensitivity. Traditionally, this challenge is solved by a wire-based readout. Two (or three) layers of wire meshes with certain wire pitch are stacked on each other with different orientations. Thus by matching recorded charge events between the multiple layers the true position can be deduced. This essentially uses multiple 2D projections to reconstruct a 3D particle interaction, and has been used sucessfully in a number of experiments. However, in high-energy and high-multiplicity environments where the interactions are more complex and there are more of them, the intrinsic ambiguities of the wire-based readout limit the event reconstruction.
The light readout in the first instance needs to be able to record, also for small tracks, a $T0$ signal. With $\sim 4 \times 10^4$ photons emitted per cm the PDE can be relatively low ($\mathcal{O}(0.1\,\%)$) to achieve this. However, the detection of VUV photons at 128 nm is not trivial and requires the application of multiple Wavelength Shifters (WLS). Commonly for this purpose PMTs are used, as they have the sensitivity to measure single photoelectrons (p.e.). PMTs coated with a WLS, that shifts VUV photons to the visible spectrum (e.g. TPB), can have a relatively high PDE ($\approx 6.5\,\%$ [64]). The main drawbacks of PMTs in LAr TPCs are the high voltage they have to be operated at ($\sim 1\,\mathrm{kV}$) and the large volume they occupy.
The cryogenic operation temperature of LAr TPCs puts further requirements on the charge and light readout, as well as on the whole detector structure. Every component needs to be able mechanically stable at cryogenic temperature. TPCs must be designed in to accommodate multiple materials with different thermal expansion characteristics that could otherwise lead to damages of the detector structure on cool down or warm up.

Chapter 4

ArgonCube Concept

Driven by the requirements of the next-generation neutrino experiments a novel LArTPC concept was developed by the ArgonCube collaboration. Common technologies used in LAr TPCs (see Chap. 3) do not fulfil the demands of future experiments and had to be replaced. The design of the detector has developed following the requirements for the DUNE ND. At the beginning of this chapter, the basic principles of the detector concept are elucidated. The needed modular design brings major challenges and requirements for the charge and light readout. Following the basic concept, it is described how these challenges were met. The tests and measurements of ArCLight conducted in this thesis were part of the prototyping phase for the DUNE ND. To put these tests in the context of the entire prototyping campaign an overview is given at the end of this chapter.

4.1 Basic concept

As described in Sec. 2.3, the next generation neutrino detectors have to be able to deal with much higher neutrino interaction rates in order to make more precise physics measurements. This brings major challenges for the ND design, since it has to mitigate pileup of neutrino events as well as beam-related background events such as rock muons. For the DUNE ND in particular, this requires completely new design approaches to LAr TPCs.
As it is unrealistic to build a LAr TPC large enough to contain all the out-going muons ($< E > \sim 3\,\mathrm{GeV}$) for the entire DUNE beam, a downstream spectrometer is used and the LAr TPC dimensions are set to contain only hadronic showers and side-going muons. The LAr TPC detector for the DUNE ND complex (ND-LAr) will have a total active volume of $5\,\mathrm{m} \times 7\,\mathrm{m} \times 3\,\mathrm{m}$ which corresponds to a total active mass of $\approx$147 t. With the beam power of 1.2 MW in the initial phase of DUNE, an average of 0.16 neutrino events per tonne of argon per 10 µs beam spill are expected in the LAr-ND [33, 65].
The ProtoDune-Single Phase (SP), a LAr TPC of similar dimension as the LAr-ND at $7.2\,\mathrm{m} \times 6.1\,\mathrm{m} \times 7.0\,\mathrm{m}$, has recently demonstrated electron lifetimes of >30 ms are achievable [66]. In a monolithic LAr TPC, it has also been shown that with access to 3D information about charge deposits will mitigate pileup to less than 0.1% for more than 50% of events, with the remaining pileup from interactions of neutral particles [67]. However, it is important to obtain a pileup-free sample of neutrino interaction, which requires the ability to tag events containing these neutral particles, predominantly fast neutrons.

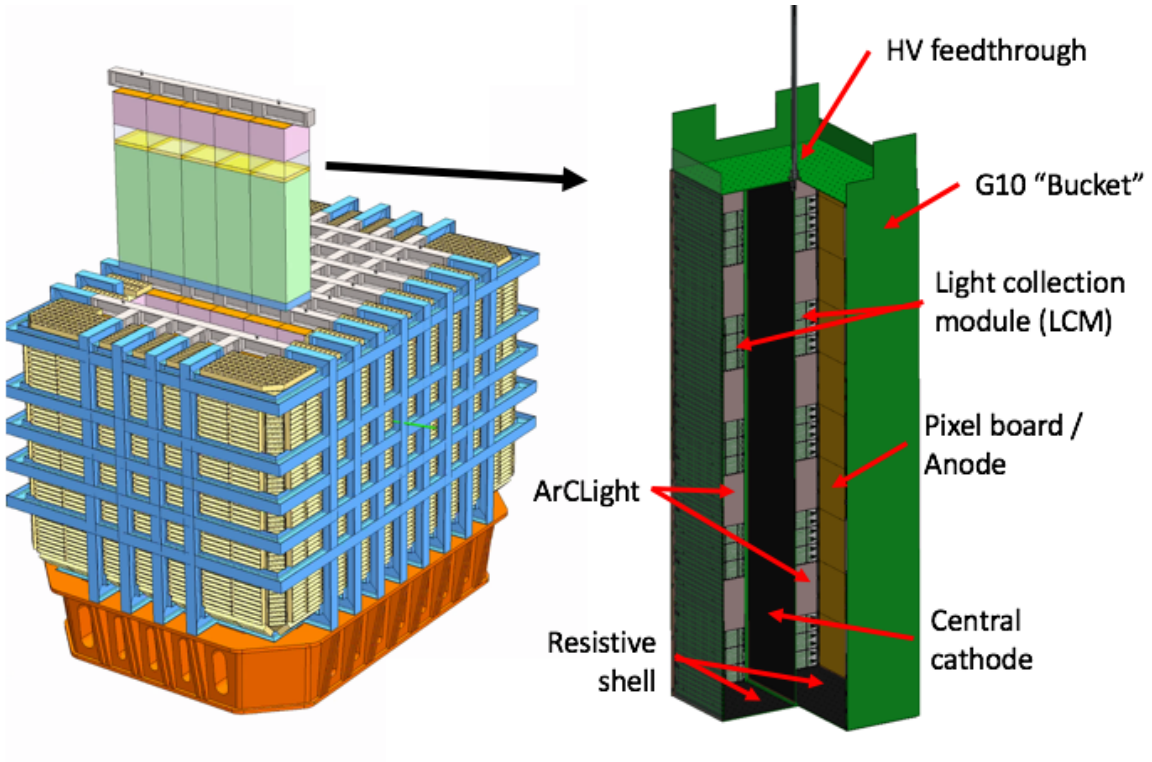

Figure 4.1 – LAr-TPC detector design for the DUNE ND (left) and cutaway drawing of a single module (right). The LAr ND consists of seven rows with five modules each. A single ND module has an active size of 1 m × 1 m × 3 m and therefore the full detector has a total active volume of 5 m × 7 m × 3 m and an active mass of 147 t.

The ArgonCube approach is a fully modular detector design, with a number of TPCs sharing a common cryostat, utilizing a pixelated charge readout. The pixelated charge readout provides unambiguous 3D images of particle interactions [68–70]. The modular design lowers the requirements on the High Voltage (HV) system, as by splitting up the full volume in several TPCs the cathode voltage can be much lower to achieve the same field strength, this also serves to reduces the stored energy per TPC and prevent damage in the case of a HV discharge. Further, due to the shorter drift lengths, the demanded electron lifetime is lower which reduces the requirements on the argon purity making the detector robust against contamination. Most importantly, the module structure is opaque meaning that scintillation light is contained within each TPC.

It is of eminent importance to be able to tag detached charge deposits caused by recoils from fast neutrons. Fast neutrons can originate from beam neutrino interactions within the active volume or the structure around it, they can travel multiple meters before causing a proton or nuclear recoil. If one of these recoils overlaps spatially with another neutrino interaction, it is not possible to distinguish them with the charge readout. The window is of $\mathcal{O}(100\,\mu s)$ and the beam spill is only 10 µs long, so all beam-related charge deposits appear as though instantaneous. For a neutrino interaction, hadronic deposits, including fast-neutron recoils, happen within a few ns of the initial interaction. Within the beam spill, neutrino interactions are separated by $\mathcal{O}(100\,ns)$. Therefore, the only possibility to tag fast neutrons is to use $\mathcal{O}(1\,ns)$ timing information, and match the recoil

to correct neutrino interaction or identify it as a beam-related external background.
The contained scintillation light of modular design allows access to the prompt component of the scintillation light. The module dimensions are set to mitigate the effect of Rayleigh scattering, which smears out photon arrival times by $\mathcal{O}(10\,\text{ns})$ for propagation distances of $\mathcal{O}(1\,\text{m})$ [52]. Since the uncertainty on the measured Rayleigh scattering length is large (see Tab. 3.1), the most conservative value has to be considered which is $\approx 55\,\text{cm}$. Fast timing not only enables temporal separation of events, but also spatial reconstruction with light, which will be discussed in Chapter 6.
An ArgonCube ND module has a $1\,\text{m} \times 1\,\text{m}$ footprint split into two TPCs with a central cathode. This gives a drift lengths of 50 cm (see Fig.4.1), which requires only a 25 kV bias to achieve a $500\,\text{V}\,\text{cm}^{-1}$ electric field. With a dielectric light readout mounted either side of the 1 m wide TPC, the maximum optical path is only 50 cm. Reducing the module footprint below this would not yield significant physics improvements, and would only increase the number of readout channels and inactive material.
The modular design and the demand to have high precision in the neutrino energy reconstruction required the development of novel readout techniques for charge and light. These are discussed in the following.

4.2 Electric Field Shaping

The uniformity of the electric field in a TPC has a major impact on the resolution of the charge reconstruction. For the modular design, a new compact approach to field shaping was needed to maximise active volume. In coarse of the ArgonCube R&D phase, a novel field-shaping technology, using a resistive shell, was developed [38]. A carbon-loaded polyimide foil replaces the conventionally used field-shaping cage structures. This technology enables a high uniformity of the electric field. The used DR8 foil[1] can directly be laminated on the G10 structure of the module minimising the amount of dead material. Further, the risk of an electric breakdown is minimised by the reducing the number of components (compared to conventional field shaping) and thus the potential points of failure. The rate of discharge is also reduced by the use of resistive material.

4.3 Charge readout

As mentioned, the commonly used wire readouts in LAr TPCs have the big drawback of ambiguities in the 3D reconstruction. This issue is solved in the ArgonCube design with a fully pixelated charge readout. The pixelated charge readout is formed of a Printed Circuit Board (PCB) and thus is mechanically robust to temperature deformation as occurring in the detector cool down and warm up. This is not the case for a traditional wire readout as slight differences in the wire tension can lead to sagging of wires, which can lead to wires touching. A fully pixelated charge readout requires amplification and digitisation of the charge signal in the cold. This is achieved by the LArPix technology [69]. LArPix is based on a system-on-a-chip Application Specific Integrated Circuit (ASIC), providing a charge-sensitive amplification and a self-triggering digitisation system. The

[1] DuPont™, DR8 polyimide film, `www.dupont.com`

current design has a pixel pitch of 4 mm in both directions. Even for EM-showering events with a large amount of induced charge over a large area, the majority of channels have no signal. Even in the intense DUNE ND environment, the expect a pixel occupancy at less than the percent level [33]. The self triggering effectively functions as zero-suppression on the ASIC level, keeping the data stream relatively low. A digital data acquisition rate of $\mathcal{O}(0.5)$ MB s^{-1} m^{-2} is expected when exposed to the flux of surface cosmic rays with a metre-scale drift length. Up to 256 ASICs can be run with a single external connection by connecting them in an optimized I/O network (Hydra I/O).

4.4 Light readout

The ArgonCube light readout has to overcome major challenges. The modular detector design requires a highly compact and dielectric light detector system that can be operated within the TPC. This makes commonly used PMTs inapplicable, as they have of relatively large volume. Further, any part placed in the drift field has to be made out of dielectric material to avoid field distortions.
As mentioned above, the light system is vital for tagging fast-neutron-induced interactions. In an event pile-up environment, this requires a fast timing ($\mathcal{O}(1\,\text{ns})$) and a certain degree of spatial resolution to match detached nuclear recoils with the corresponding event ($\mathcal{O}(10\,\text{cm})$) [71].
To meet these requirements two separate large area light detection systems were developed. The Light Collection Module (LCM) panel developed by JINR uses a bundle of WLS fibres [72]. These fibres are placed on a PVC plate and are connected on each end to a SiPM. The WLS fibres are coated with 1,1,4,4-tetraphenyl-1,3-butadiene (TPB) that serves as a VUV WLS. This design shows a relatively high PDE of $\approx$1 %. But since all fibres are connected to the same two SiPMs, the spatial resolution is limited to the size of a single panel (10 cm $\times$ 30 cm).
The requirement of a high enough spatial resolution is realised by the ArCLight detector developed by the University of Bern. Its design is based on dielectric WLS plate used as a light trap that is coupled to SiPMs. The design is discussed in detail in Sec. 5.1. Furthermore, it is extensively tested to confirm the aforementioned requirements are fulfilled.

4.5 Prototyping plan for DUNE near detector

This thesis is part of the several-years' prototyping campaign for the implementation of ArgonCube in the DUNE ND. In the following, an overview of this prototyping campaign is given. It can be split up into two main phases.
In the first phase, the single components are produced and tested. These tests could be performed in small-scale setups and took place in the different institutes as part of the ArgonCube R&D program. Especially, the novel techniques developed for this detector design, e.g. LArPix, the resistive shell, ArCLight and LCM, underwent a intensive component-level prototyping [38, 69, 72, 73]. This phase was successfully completed by summer 2020.

The second phase is the integration-level prototyping. It demands more complex infrastructure and is therefore condensed on three main test setups.
The first setup, called SingleCube, represents a single "cell" of the final detector design. This smallest unit consists of one LArPix pixel board (32 cm × 32 cm) and one light readout unit. A light readout unit consists either of 3 LCM panels or one ArCLight panel. Here, the resistive shell is not implemented yet, instead a field cage formed traces on a PCB is used (for details see Sec. 6.2). With this setup, the basic level combination of charge and light readout can be tested. The first SingleCube test was performed in October 2020 at the University of Bern.
In a second setup a full prototype module, called Module 0 (Mod 0), is implemented. This prototype module is a downscaled version of the module as it will be implemented for the final DUNE ND design. The drift length is reduced to 60 % of the final 50 cm, and the height to 40 % of the final 3 m. Here, for the first time, the light and charge readouts are implemented within the resistive shell TPC. Further, this represents also the first test of the large scale resistive shell technology. As the charge readout components were delayed, for a preliminary test the Mod 0 is only equipped with a single readout cell as in SingleCube plus one additional light readout (see Sec. 6.2). This test allowed to confirm the functionality and stability of the HV system and the resistive shell. It was completed in December 2020. Later, a fully equipped module will be tested. This enables the test of the interoperability of 16 pixel boards and 16 light units. The Mod 0 tests are planned to be finished by April 2021 and will be carried out at the University of Bern.
These first two setups are limited to cosmic radiation data. They will not be placed in

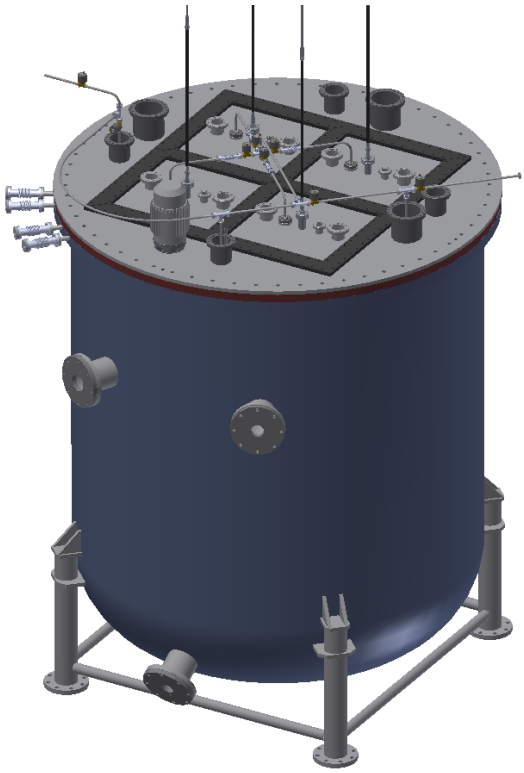

Figure 4.2 – Drawing of the ArgonCube 2x2 demonstrator. The demonstrator consists of 4 modules with a size of 67 cm × 67 cm × 181 cm each.

any test beam.
The final setup is a 2x2 module demonstrator [74]. It represents the first test of the integration of multiple modules. The four modules are of the same size as Mod 0. A CAD drawing of the demonstrator is seen in Fig. 4.2. The demonstrator will undergo intensive testing and will be placed in the MINOS ND hall at Fermilab. The 2x2 will form part of the ProtoDune-ND [75] together with tracking and calorimeter components of MINERvA [76]. ProtoDUNE-ND will be exposed to the NuMI neutrino beam [77]. The setup enables to test beam neutrino event reconstruction across multiple modules and multiple detector types. A first run of the 2x2 demonstrator is planned to be completed by April 2022.

Chapter 5

Development and Production of ArCLight

This chapter presents the concept and development of the ArCLight light detector based on the requirements discussed in the previous chapter. The developments discussed here build upon the already existing version of ArCLight as described in Auger et al. [73].
In the first part, the functional principle and design of the existing design version are explained. Based on several tests at cryogenic temperatures different design changes were applied. The production and the implementation of these changes are discussed in the second section of this chapter. A major issue discovered by these tests was the quality of the WLS coating, this led to the development of a novel coating setup which is described in the last section.

5.1 The ArCLight detection principle and original design

The requirements for the ArgonCube light readout as discussed in Section 4.4, led to the design of a novel light readout system, since the typically used PMTs are not applicable in the ArgonCube concept. The ArCLight design was inspired by the ARAPUCA light trap sensor [78]. An overview of how the light trapping is achieved in the ArCLight design is shown in Fig. 5.1 and described step-by-step in the following. In this section, only the existing design as developed in Auger et al. [73] is described.
In order to enable the trapping of photons in a cavity the inner surfaces need to be highly reflective for the considered wavelength. There is no such material working for the wavelength of LAr scintillation light. Therefore the scintillation light wavelength first has to be shifted to a regime that is convenient.
For this purpose, TPB is commonly used. TPB is an organic chemical compound that shifts 128 nm light to around 430 nm in the visible spectrum (see Fig. 5.2). The absorption length of this process is (400 ± 75) nm and it has a quantum efficiency of (0.475 ± 0.025). The maximum efficiency is reached at a layer thickness of $\approx 3\,\mu$m [79].
The sensitive surface of the detector panel has to be transparent to the light emitted by TPB. In order to prevent photons entering the cavity from exiting it, they have yet to be shifted to another wavelength for which the entrance surface is not transparent. In

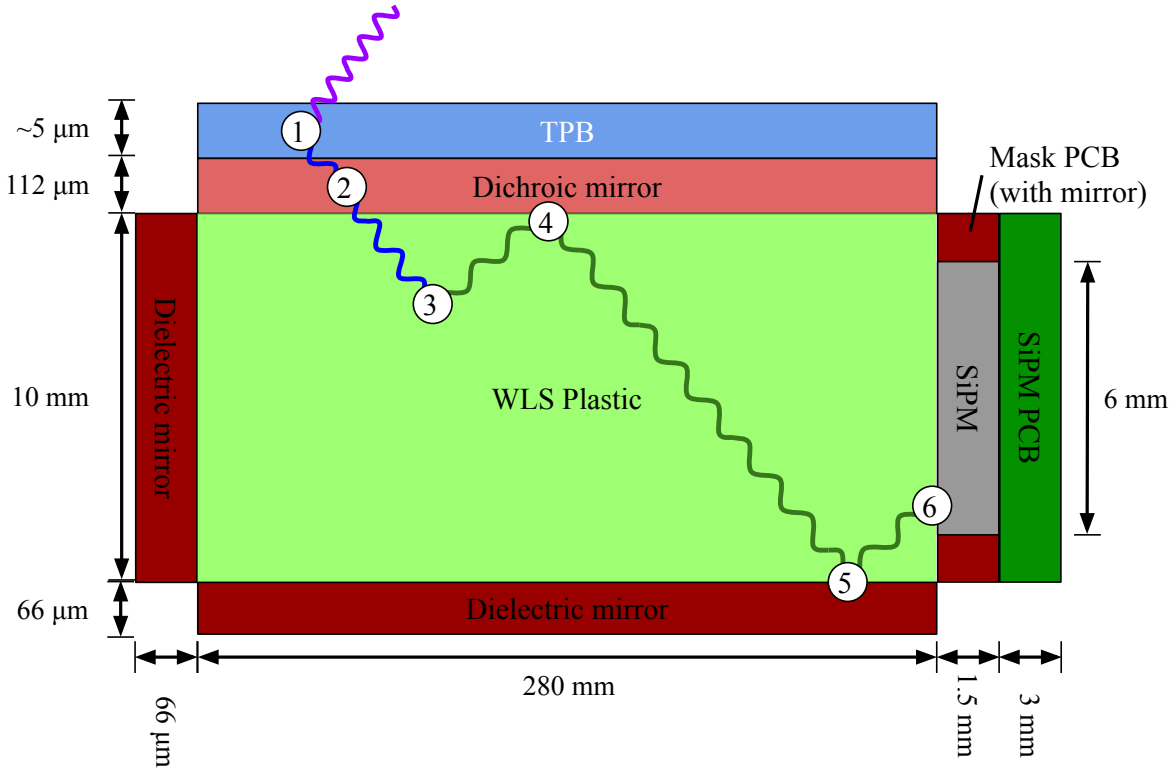

Figure 5.1 – Schematic profile of ArCLight with dimensions for the ArgonCube 2x2 demonstrator. The total size of the WLS plastic is 30 cm x 28 cm x 1 cm. An incident photon goes through the following steps: (1) Incoming VUV photon (∼128 nm) gets shifted to blue (∼430 nm) by TPB, (2) Blue photon can penetrate through the dichroic mirror, (3) Blue photon gets shifted to green (∼490 nm), (4) Green photon gets reflected by dichroic mirror, (5) Green photon gets reflected by dielectric mirror, (6) Photon hits Silicon Photo Multiplier which is mounted on a Printed Circuit Board and produces an electrical signal.

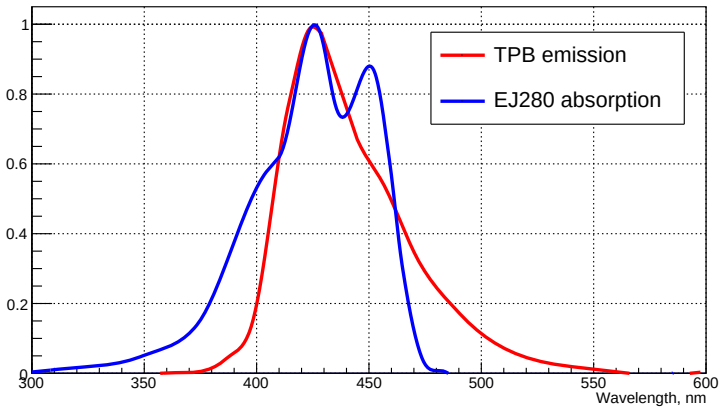

Figure 5.2 – Emission spectrum of TPB and absorption spectrum of the EJ280 WLS plastic (in a.u.) [73]. The two spectra are largely overlapping which leads to a high photon conversion efficiency from VUV to green.

the ArCLight design, the WLS plastic EJ280 produced by Eljen Technology is used for this purpose. EJ280 shifts the incoming blue photons from TPB to green (see Fig. 5.3) with a average efficiency of 86% [80]. Since this WLS plastic is self-supporting, it also servers as the main structure of ArCLight. The WLS absorption spectrum of the WLS plastic depicted in Fig. 5.2 is highly overlapping with the TPB emission spectrum which leads to a high conversion efficiency of VUV photons to green. The absorption length of EJ280 was determined by measuring the absorbance for two samples of thickness 3.5 mm and 9.2 mm. The results of these measurements can be seen in Fig. 5.4.

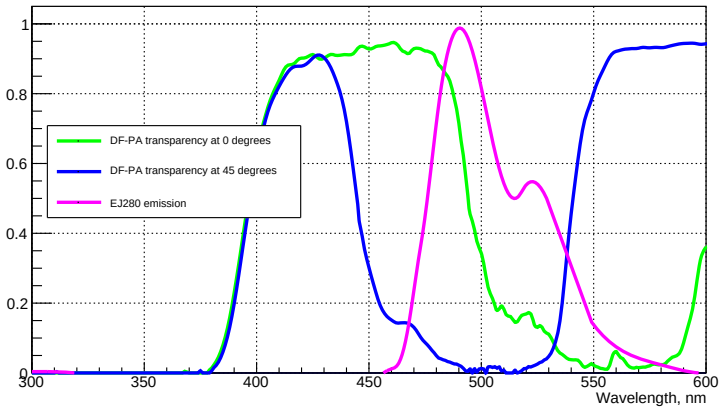

Figure 5.3 – Transparency of DF-PA dichroic for 0° / 45° incident angle and emission spectrum of the EJ280 WLS plastic (in a.u.)[73]. The EJ280 emission spectrum overlaps only for low incident angles with the transparency window of the dichroic.

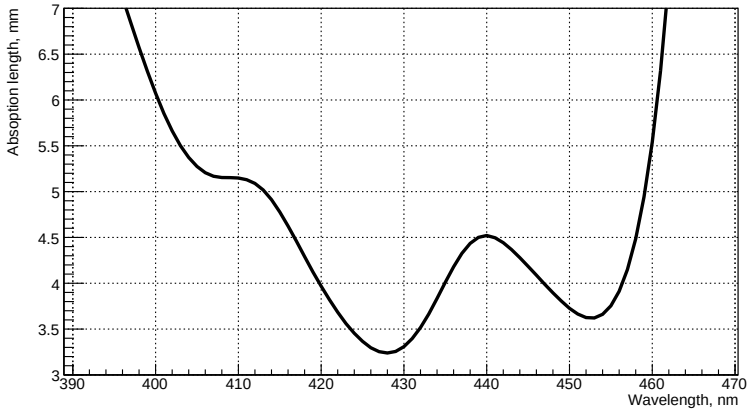

Figure 5.4 – Measured absorption length of the EJ280 WLS plastic. The absorption length reaches a minimum of 3.24 mmat a wavelength of 428 nm.

At the sensitive surface of the detector, a self-adhesive dichroic mirror foil is placed. This prevents the photons emitted by the WLS plastic leaving the structure. The 3M DF-PA Chill foil used has the property that the TPB-emission light can transmit but green light is reflected. The TPB is coated directly on the dichroic mirror. The TPB emission spectrum highly overlaps with the transparency window of the dichroic mirror as seen

in Fig. 5.5. Thus, photons emitted by the TPB layer can transmit through the dichroic mirror into the WLS plastic. In Fig. 5.3, it is shown that the transparency window of the dichroic mirror overlaps with the WLS plastic emission only at very low angles of incidence preventing green photons from leaving the cavity.

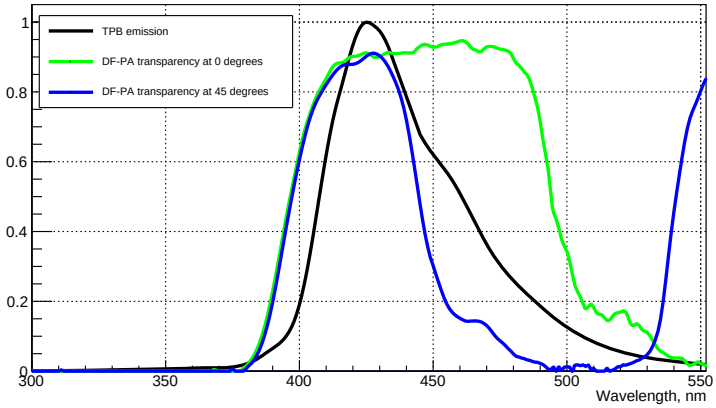

Figure 5.5 – DF-PA dichroic transparency for 0° / 45° incident angle and emission spectrum of TPB (in a.u.)[73]. The EJ280 emission spectrum overlaps only for low incident angles with the transparency window of the dichroic.

The non-sensitive surfaces, up to the one where the Silicon Photomultipliers (SiPMs) will be placed, need to be reflective for photons in the emission spectrum of the WLS plastic. This is achieved by coating these surfaces with a mirror foil. Here the 3M Vikuiti™ Enhanced Specular Reflector (ESR) foil is used, which has a reflectivity of $\geq 98\,\%$ in the considered spectrum range [81]. This foil was attached to the WLS plastic by using an adhesive layer (3M 200MP).
Finally, the trapped photons are detected by one of the six SiPMs attached to the WLS plastic. Here Hamamatsu S13360-6050CS SiPMs with a larger sensitive area of $6\,\text{mm} \times 6\,\text{mm}$ are used [82]. These have a PDE of $\approx 38\,\%$ in the range of the WLS plastic emission spectrum.

5.2 Production and structure cold tests

In comparison to the former versions of ArCLight, the goal for this thesis was to scale the existing design up to the size as it will be used for the ArgonCube 2x2 demonstrator. Therefore, the whole production process had to be enhanced and several design aspects had to be changed. The dimensions of the ArCLight version tested in this thesis are depicted in Fig. 5.1 except the depth which is 30 cm for the WLS plastic. These dimensions are following the requirements for the ArgonCube 2x2 demonstrator (see Section 4.5). The panel has a sensitive area (TPB coated surface) of $28\,\text{cm} \times 30\,\text{cm}$. Following the calculations in Auger et al. [73] with the properties of the current version of ArCLight, assuming a uniform TPB coating and considering a corrected value for the TPB efficiency [79], one gets an expected overall PDE of $(0.27 \pm 0.16)\%$. The size of the panel will be increased to a sensitive area of $50\,\text{cm} \times 30\,\text{cm}$ for the ArgonCube ND design.

For a first test, an ArCLight panel was produced based on the former design described in the previous section. To assess the structural stability during thermal contraction, tests at cryogenic temperatures were performed. The panel was cooled down to liquid nitrogen (LN2) temperature (77 K) during a period of 4h (75 K/h). In this test the mirror foil detached from the WLS plastic at a temperature of ≈ 200 K due to slight differences in the thermal expansion coefficient. This problem did not occur in previous tests of the ArCLight panels, which were of smaller size (10x10 cm^2 and 10x30 cm^2). On the other hand, the dichroic foil stayed attached although it has similar thermal contraction properties as the mirror foil. In the following, a test series was conducted where the adhesive layer keeping the mirror foil in place, was replaced by epoxy or silicone glue. Furthermore, a test with single strips of the adhesive film and a version where the adhesive layer was heated during the lamination process were conducted. All of these tests failed on contact of the panel with LN2.

In the course of the above-mentioned test series also the lamination process was improved. Cold lamination rollers with adjustable force were applied. During the lamination, the panel was heated with a heat gun to improve adhesion.

For a last cold test, the 3M Vikuiti™ ESR foil was replaced with the 3M DF2000 foil which, as the dichroic foil, has a prefabricated adhesive layer on it. The cool-down test for this setup was successful. The mirror foil remained attached and did not show any instability. However, this cool-down test did not prove the long term structural rigidity. Thus, during a test of a LAr filtration system the ArCLight panel was kept for a full week at liquid argon temperature (85 K). This test showed first signs of fragility, as the mirror foil detached primarily at the lateral surface. During a second week in cold the mirror foil detached completely.

As a consequence of the issues with the adhesion of the mirror foil, a version of the ArCLight structure without mirror foil was studied. On the surface, where the SiPM are placed, the foil is held in place by the Mask PCB (see Fig. 5.1). Thus, this is the only surface where the mirror foil was retained. This design is fully relying on the internal reflection due to the difference in refractive index between the WLS plastic and LAr (1.58 and 1.25 respectively) at 430 nm. The reflection properties of this interface as described by the Fresnel equations are shown in Fig. 5.6. Total internal reflection occurs for angles of incidence larger than 52.3°. Thus, one expects a drop in PDE for this version of ArCLight, but it also shows good long-term structural stability.

A further issue of stability is the difference in the thermal contraction of the WLS plastic and the PCB supporting the SiPMs. The WLS plastic has a coefficient of linear expansion of $7.8 \times 10^{-4}\,K^{-1}$ which leads to a total contraction of ≈ 5 mm along the side where the SiPM PCB is mounted. The thermal contraction of the PCB is negligible. Thus, the SiPM PCB mounting is designed to allow it to be able to slide with respect to the WLS plastic.

A fully assembled ArCLight panel (without mirror foil) can be seen in Fig. 5.7. The two design versions, with and without mirror foil, were extensively tested in a test setup with a TPC. The setup and results for these tests are discussed in Chapter 6. During these tests, also replacing of the mirror foil with the dichroic mirror was tested. However, the impact of this design change was not studied separately as the impact of the mirror foil on the PDE was found to be minor.

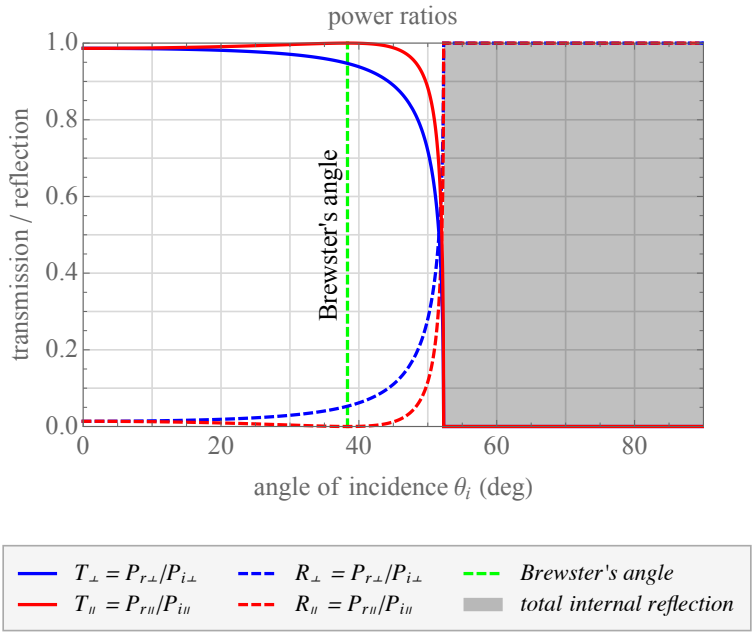

Figure 5.6 – Reflection properties of the WLS plastic to LAr interface. The reflectivity and transparency for angles of incidence from 0° to 90° are calculated following the Fresnel equations. Total internal refection takes place above 52.3°. Plot based on [83].

5.3 Wavelength shifter coating for ArCLight

In the former versions of ArCLight, the TPB was deposited by airbrush on the dichroic mirror. The TPB was dissolved together with polystyrene in toluene and sprayed on as a solution. This leads to a structure of TPB crystals embedded in polystyrene and improves the robustness of the TPB layer to wash off by LAr. However, by inspecting the TPB layer under a microscope it becomes apparent that the coverage factor of TPB is relatively poor (see Fig. 5.8a).

As stated in Benson, Gann, and Gehman [79], switching to evaporation deposition increases the coverage massively. In evaporation deposition the substrate coating (here TPB) is vaporized in a vacuum using a heat source. The flux of vaporized substrate eventually hits the target surface, where it condenses. Since the target, in this case, is relatively large, commercial evaporators are not applicable. Thus an evaporation chamber suitable for ArCLight was developed and tested.

The developed evaporation chamber is equipped with a large surface heater table and a sample holder. In Fig. 5.9 a drawing of the inner structure and a picture of the entire setup are seen. The used vacuum chamber is a box-shaped acrylic chamber from Cleatech LLC [84]. The chamber is pumped with a two stage pumping station consisting of a rotary vane and a turbo molecular pump. To achieve a highly uniform coating, the TPB is dispersed on an aluminium tray of the size of an ArCLight panel. This tray is placed on a heater table that is heated with nine power resistors (50W each). The temperature of the heater kept constant with a PID controller. A support structure with a variably adjustable distance to the heater table is used to hold the substrate. A water-cooled

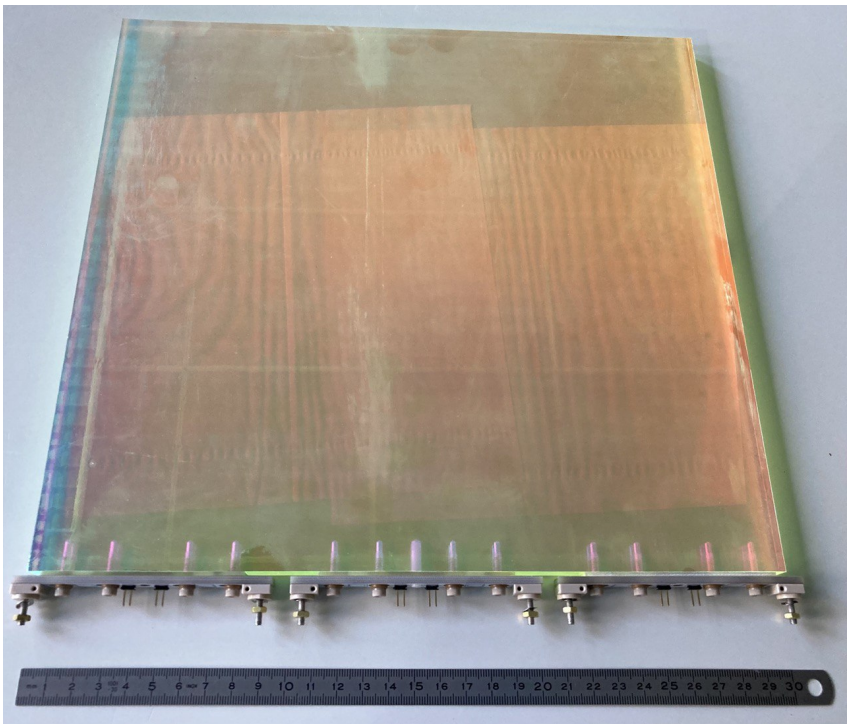

Figure 5.7 – ArClight version without mirror foil with sensitive area of 28x30 cm^2. On the lower edge the mounted SiPM PCBs are seen with bolts for mounting into a TPC system. The TPB coating on the apparent surface is applied by air brush.

aluminium plate is placed on the top of the substrate to prevent overheating.
Two different coating procedures were tested. In a first study, the dichroic mirror foil was laminated to the WLS plastic and then put into the evaporation chamber. The obtained coating is seen in Fig. 5.8b. It has a coverage factor of almost 100 % and is relatively robust. However, due to the low thermal conductivity of the WLS plastic, the cooling from the backside is not very effective on the side that is exposed to the thermal radiation of the heater table. This leads to major delamination of the dichroic foil form the WLS plastic.
To avoid this issue, a second procedure was tested where only the dichroic mirror foil itself has been put into the evaporation chamber. Therefore, the cooling is much more effective since the foil is directly attached to the cooling plate preventing the adhesive from melting. The coated foil is then laminated on to the WLS plastic. This procedure leads to a more robust adhesion of the dichroic foil to the WLS plastic, which is necessary to prevent it from getting detached during the cool down to LAr temperature.
The thickness of the coating was optimised to 3 µm, which leads to the high achievable WLS efficiency [79]. The PDE of the ArCLight with the two different coatings is compared in Chapter 6.
In summary, the changes in the design and production procedure provide a more robust structure. The removing of the mirror foil causes a drop in the PDE. However, due to the improved TPB coating an improved performance is expected.

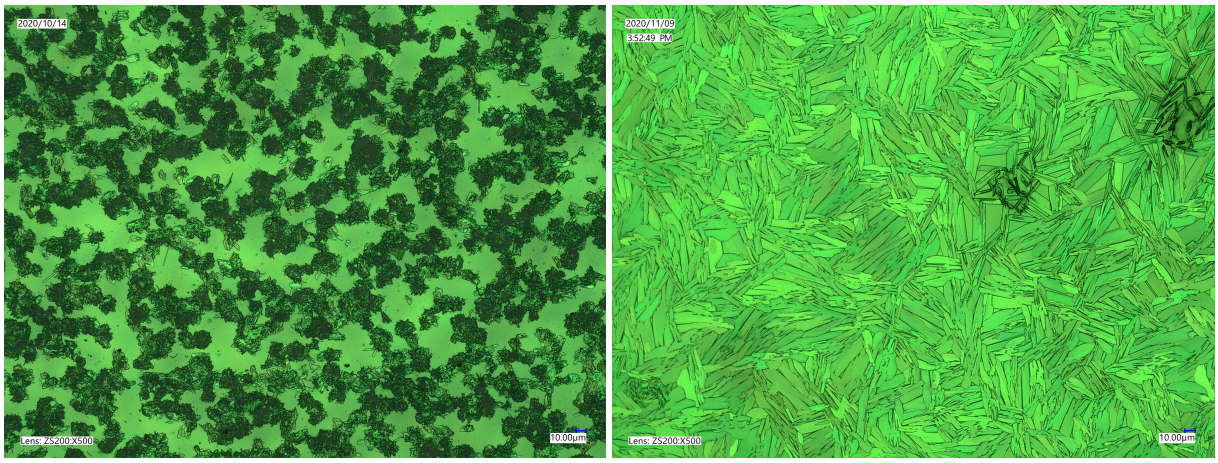

(a) Air brush **(b)** Evaporation deposition

Figure 5.8 – Microscopic images of the TPB layer achieved with air brush (left) and evaporation deposition (right). The magnification for both images is ×500.

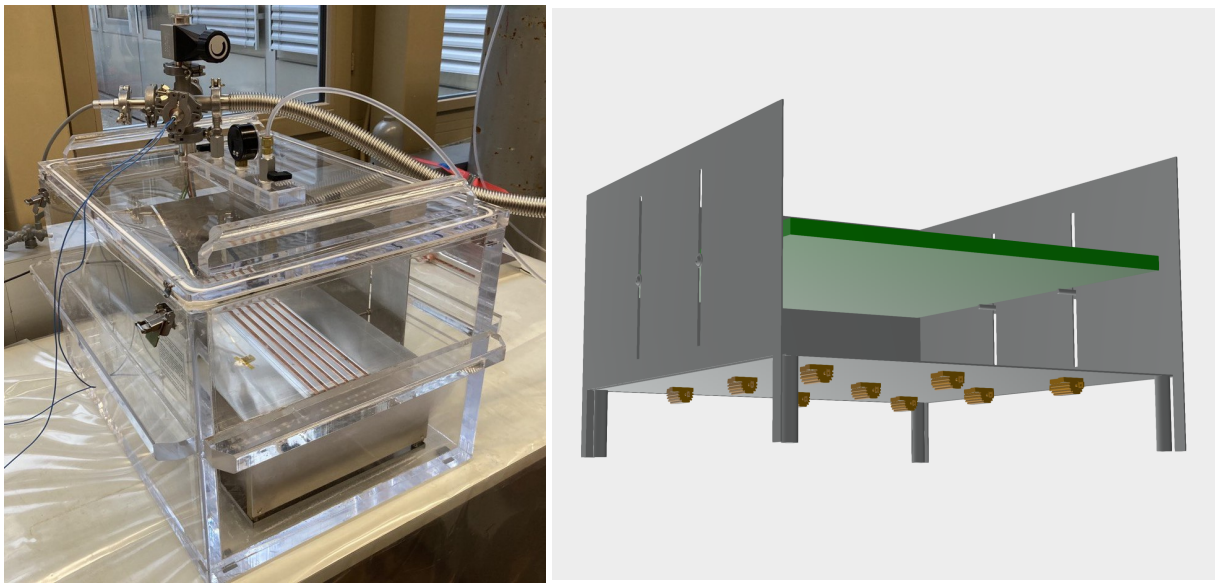

(a) **(b)**

Figure 5.9 – Evaporation chamber setup. (a) Picture of the acrylic vacuum chamber with evaporation setup inside and all feedthroughs connected. (b) CAD drawing of the heater table with the power resistors (orange) and the sample support structure.

Chapter 6

Characterisation of ArCLight performance

In the previous chapter different changes in the ArCLight design were discussed, which lead to changes in the performance of ArCLight. In this chapter, the impact of the design changes on the PDE are quantified. Before conducting the actual measurements an optical simulation is performed. For the measurement of the performance different test runs were conducted. The test setups, the signal readout, and calibration procedure are all described. By applying a reconstruction algorithm on the collected data, a first estimator of the spatial resolution in one coordinate direction is determined. Finally, the measured PDE is used to set an energy threshold level for the tagging of neutron-induced recoils with ArCLight.

6.1 Simulation studies of the optical performance

During the development of the ArCLight design changes as described in Chap. 5, an optical simulation was set up to get a preliminary estimate of their impact on the PDE. Furthermore, this simulation was used to establish an algorithm for the spatial reconstruction of the photon emission on real data for ArCLight. The simulation is based on GEANT4 and builds up on an existing optical simulation for ArgonCube with a preliminary implementation of ArCLight. The same simulation is used to produce a lookup table for the whole light readout system of ArgonCube.
As this thesis focuses on the performance of ArCLight, a separate simulation was set up where only the ArCLight system is studied, instead of a full ArgonCube module. The two different versions of ArCLight, with and without mirror foil, were implemented in GEANT4. All optical properties were set with the parameters described in 5.1. This included refractive indices of all materials, reflectivity and transparency properties of all optical interfaces (angular dependent for dichroic foil), as well as WLS and absorption properties of all materials. The TPB coating was approximated as a uniform layer of 3 µm thickness with a rough surface (as achieved by evaporation coating).
In the simulations, photons with a 128 nm wavelength were generated uniformly distributed 1 µm above the TPB layer in a LAr volume. At each of the 10k emission points, 100k photons were generated. Only photons that hit a SiPM (and do not get reflected) were recorded. For each of these photons, the energy dependent SiPM sensitivity was

considered and the average number of produced photo electrons (p.e.) for each emission point was calculated.
The PDE was deduced as the fraction of the number of measured p.e. versus the number of emitted photons for each emission point. The overall PDE results for the two ArCLight versions are shown in Fig. 6.1. The average PDE is $(0.0352 \pm 0.0011)\,\%$ for the version without mirror and $(0.1006 \pm 0.0032)\,\%$ for for the version with mirror. I.e. the overall PDE drops by a factor 2.86 ± 0.13 when removing the mirror foil in the simulation.

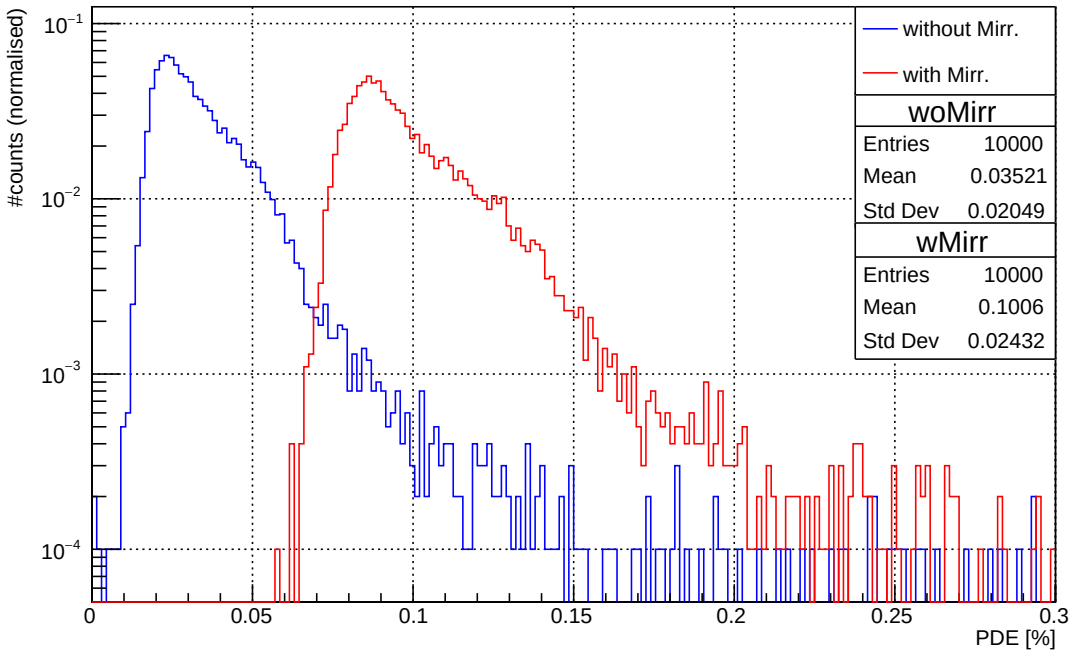

Figure 6.1 – Simulated overall PDE distribution of two ArCLight versions with and without mirror foil.

In the spatial dependence of the PDE, on the point where the photons hit the sensitive surface of the panel, no differences are observable between the two versions. Fig.6.2 shows the spatial dependence of the PDE for the version without mirror foil. The PDE is as expected higher close to the SiPMs but drops at the very edge of the panel in-between the SiPMs.
As mentioned in Sec. 4.4, the goal of ArCLight is to provide a spatial resolution that enables a rough determination of the light emission point and therefore the matching of track and light signals in case of a event pile up. In this thesis only conservative methods (no artificial intelligence (AI)) were used in the reconstruction of the spatial coordinates. The spatial resolution is defined as the Root Mean Squared Error (RMSE) of the variable $\delta x^i = (x^i_{meas} - x^i_{true})$, where x^i_{meas} and x^i_{true} are the measured/reconstructed and true value for the x^i coordinate of the emission point and x^i_{true} respectively.
For the reconstruction of the y coordinate (see 6.6b for definition of directions) different attempts were made to get a precise and robust algorithm that calculates y_{meas} from the available information. The reconstruction has to be based on the distribution of the measured number of p.e. for each SiPM for a single event, as this is the only information

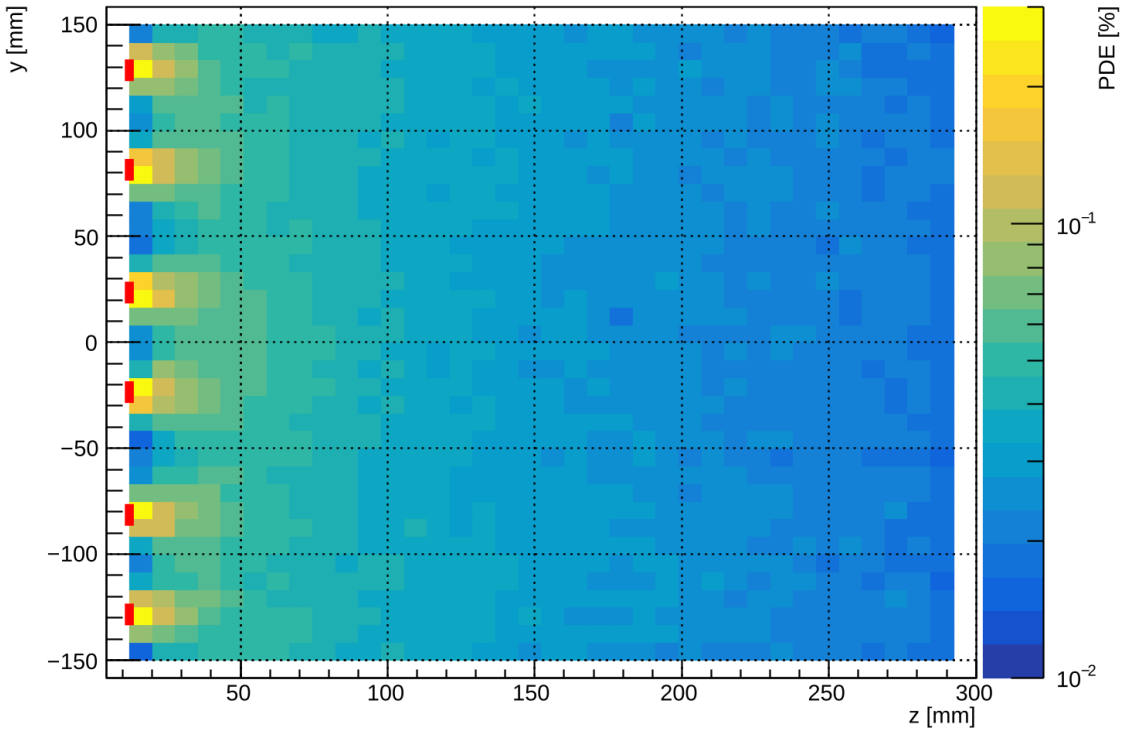

Figure 6.2 – PDE dependence on the entry point of the photons at the sensitive surface of ArCLight without mirror foil. The SiPM positions are marked with red.

available in the experimental data. The most robust approach found is to take the centre of this distribution calculated as

$$\tilde{y}_{meas} = \frac{\sum_{i=1}^{6} (n_i p_i^y)}{\sum_{i=1}^{6} n_i}, \tag{6.1}$$

where n_i is the number of measured p.e. in the i-th SiPM and p_i^y is the y coordinate of the i-th SiPM. However, $\tilde{y}_{meas}$ has to be scaled by a factor of 1.8 in order to minimize δy and get a 1 to 1 correlation between y_{meas} and y_{true}. The following results are obtained for a ArCLight without mirror foil. In Fig. 6.3 the result of the reconstruction algorithm are shown. For the entries in each y_{true} bin, the spatial is determined by calculating the RMSE. The chosen reconstruction approach does not give a perfect unbiased result and δy shows a y-dependent systematic offset. These results are depicted in Fig. 6.4. For the outer part of the detector (y>100 mm or y< − 100 mm), the systematic offset and the resolution are significantly worse than in the inner part of the panel. The chosen reconstruction method starts to fail close to the outermost SiPM positions. This edge effect will get partly solved if multiple panels are placed next to each other and when one can look at the p.e. distribution over multiple panels. For the inner part of the detector an average resolution of (17.41 ± 0.34) mm is expected.
For the z direction (see 6.6b), any attempts for a conservative reconstruction failed. This may be only achieved with more sophisticated algorithms including AI methods.

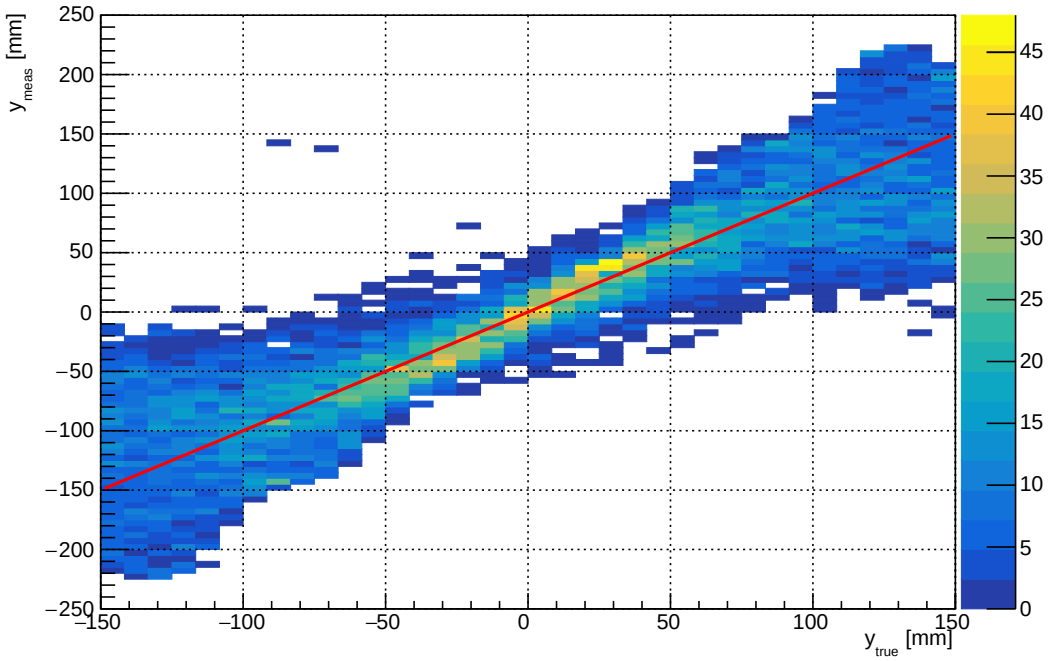

Figure 6.3 – Performance of the y coordinate reconstruction of the photon emission point in the optical simulation. The red line indicates the intended 1 to 1 correlation between the measured and true position.

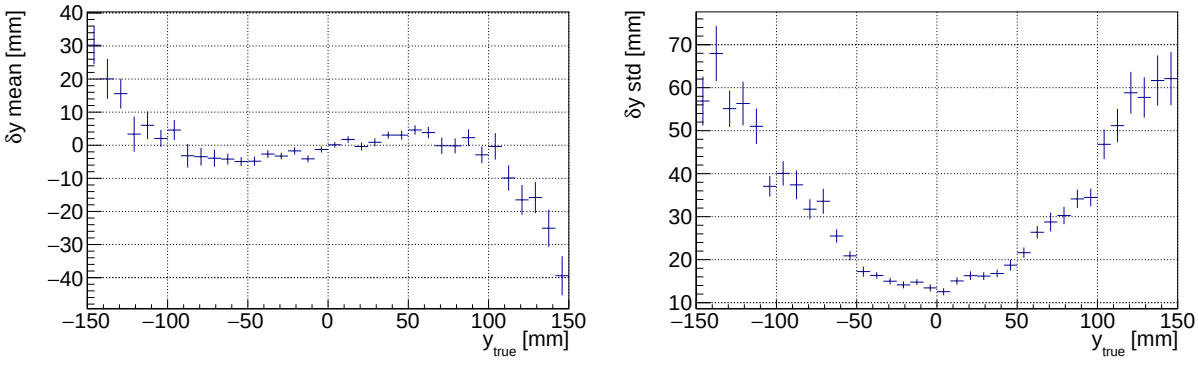

(a) **(b)**

Figure 6.4 – Systematic offset (a) and spatial resolution (b) of the y coordinate reconstruction in the optical simulation.

6.2 Test stand setups

To measure the performance parameters of ArCLight, four different test setups were used in total. In Tab. 6.1 an overview over the test runs is given and the parameters of the used ArCLight panels are listed. These tests are part of the prototyping plan for the DUNE ND (see Section 4.5). PurityRun I and II are part of the component-level phase, as SingleCube and Mod 0 are part of the integration-level phase. In the following, the setups are described in detail.

Table 6.1 – Overview over the test runs used for the light readout characterisation. Except for the SingleCube run, two light readout panels could be placed in the detector. In course of the DUNE ND prototyping, LCM modules were also installed but they will not be discussed in this thesis.

Run name	TPC drift length [cm]	Light r/o I			Light r/o II		
		Name	TPB coating	Mirror foil	Name	TPB coating	Mirror foil
PurityRun I	18.5	ArCLight	Airbrush	Yes	LCM	Paintbrush	-
PurityRun II	18.5	ArCLight	Airbrush	Yes[1]	ArCLight	Airbrush	No
SingleCube	30	ArCLight	Airbrush	No	None	-	-
Mod 0 HV test	30	LCM	Paintbrush	-	ArCLight	Evaporated	Yes[2]

[1] Mirror foil detached during run.
[2] A dichroic mirror foil was placed on the panel backside.

The first two test runs, PurityRun I and II, were performed in a 300 l cryostat and had the main purpose to test the argon purification system developed at the University of Bern. However, as both of these runs the cryostat was equipped with a TPC, they could be utilised to test the light readout system with ArCLight. The same cylindrical TPC developed for the pixel initial tests [68] was used for both runs (see Fig. 6.5). The TPC is built up of 10 field shaping rings (diameter 10 cm) and has a total length from cathode to anode of 18.5 cm. The charge readout is realised by a multiplexed pixel board (28 regions of interest, 36 pixels each) connected to LArASICs (for a full description see [68]). Additionally, a muon telescope is used which is built up of two 7.5 cm × 7.5 cm × 0.5 cm scintillator plates. If a coincidence of the two occurs, both charge and light readout get triggered.
In PurityRun I, carried out in March 2020, an ArCLight panel with mirror foil and airbrush coating was tested. The panel was mounted next to the TPC with the cold amplifier board (see 6.3) on the top side. The main focus of this run was to test the long term stability of the ArCLight panel at LAr temperature, these results are discussed in Section 5. The cryostat was filled with LAr for 7 days. As the readout electronics were installed the first time in Bern, this run was also used to test the entire light readout chain. Furthermore, a temporary internal LAr purification system was employed. The purity achieved in this run was high enough to be able to neglect light attenuation due to impurities. In PurityRun II, carried out in July 2020, two different versions of ArCLight were compared, one with and one without mirror foil, both had an airbrush TPB coating. The whole run lasted 9 days with 6 days of data taking. For the first time, the 2x2 external LAr filtering system was tested, which allowed reaching a higher purity (≈0.5 ms electron lifetime) than in the previous tests.

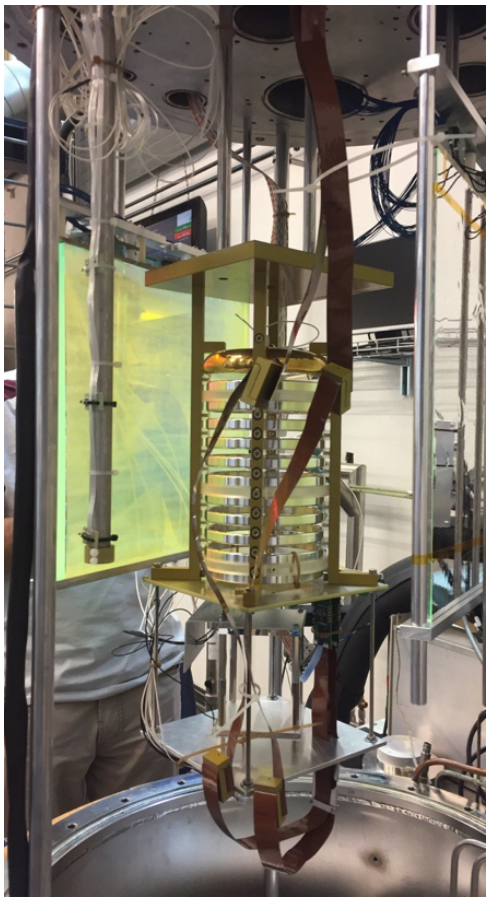

Figure 6.5 – Detector setup for PurityRun II. Below the 18.5 cm ring shaped TPC the scintillator based muon telescope is placed. Two ArCLight panels (with and without mirror foil) are placed parallel to each other around the TPC.

In October 2020 a third test run was conducted in the same 300 l cryostat. The used SingleCube TPC (depicted in Fig. 6.6a) is based on a fully pixelated charge readout with LArPix V2 ASICs [69]. The cubic PCB structure is equipped with 60 conductive strips connected with a resistor chain which achieved a good field uniformity. The pixel PCB was equipped with an array of 10x10 ASICS and 4900 pixels in total. The ArCLight panel without a mirror foil, used already in the previous test run, was transferred to the SingleCube. It was held in perpendicular position to the pixel plane by a G10 structure, as in the 2x2 design.

The first single module (Mod 0) for the 2x2 demonstrator was tested in November 2020 in a HV test. It was tested in a 1500 L cryostat connected to the external filter cryostat already used in the previous runs. The module has an active volume of 64 cm × 64 cm × 120 cm with a central cathode plane splitting it up to two separate TPCs, so the maximum drift length is 32cm. The electric field is build up with a resistive shell laminated directly on the G10 structure of the module. The fully assembled module is seen in Fig. 6.7a. For this test run only a single pixel PCB (10x10 ASICs) with an active area of 30 cm × 30 cm was inserted. Next to the pixel PCB a set of 3 LCM panels was installed. An ArCLight version coated with TPB by evaporation was placed next to them (see Fig. 6.7b). This ArCLight was equipped with a dichroic mirror foil (of the same type

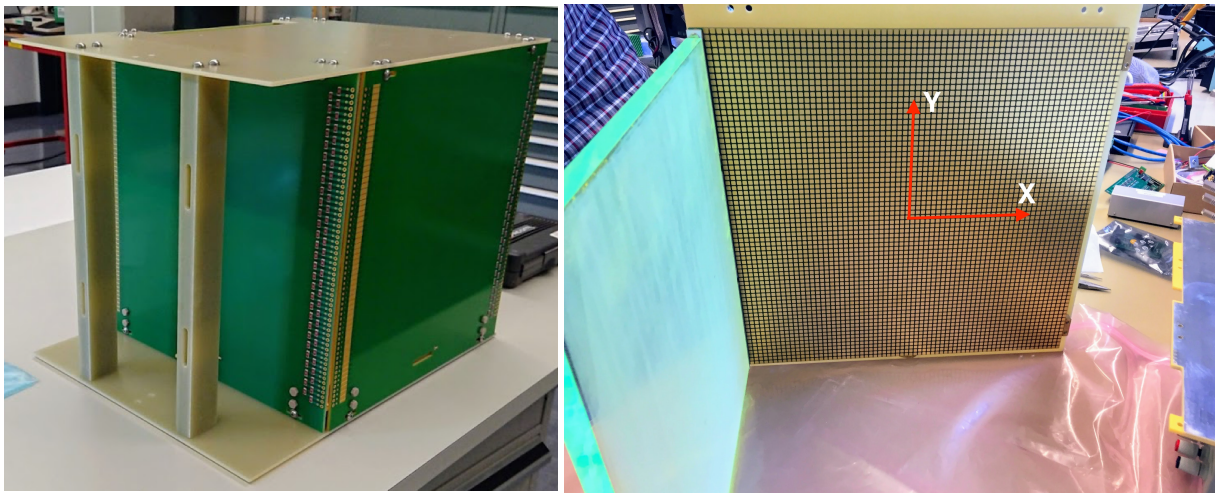

(a) **(b)**

Figure 6.6 – Setup of the SingleCube detector: (a) Field cage built up of PCBs (green) mounted to a G10 support structure. The resistor chain, connected to the conductive strips on the inner side of the PCBs, is seen in the centre of the picture. (b) LArPix V2 pixel PCB and ArCLight mounted on a G10 support plate. The coordinate axis as used for the analysis are depicted. The z axis lies perpendicular to the pixel PCB parallel to the ArCLight surface.

as on the sensitive surface) on the non-sensitive surface next to the field shell, this was done as the lamination of the dichroic mirror foil was tested to be robust compared with the standard fully reflective mirror foil.

6.3 Light readout electronics and calibration

The light readout electronics were developed and produced by JINR and are discussed in detail in Anfimov et al. [72]. For reasons of completeness, a summary is given in the following. The purpose of the readout electronics is to amplify and digitise the analogue signal generated at the SiPMs of the light detector. Up to 6 SiPMs are directly connected to one so-called E-board (E shaped PCB). On this board, for each channel, a separate preamplifier is placed to produce a large enough signal to transmit to the next amplifier stage. The preamplifiers have a rise time of ≈10 ns which enables fast timing information as required (see 4.4). The next amplifier stage is placed outside the cryostat and has a variable gain setting. It also transforms the unipolar signal from the preamplifiers to a differential signal. The differential signal is then transmitted to the Analogue-to-Digital Converter (ADC) stage. The SiPM bias voltage is provided by a channel-by-channel adjustable voltage distributor. The voltage distributor is fed with a common bias voltage of ≈60 V, for cold operation.
The ADC stage has 64 channels for each unit, with a 10 bit resolution in the full range of ±1.25 V and runs at a sample frequency of 100 MHz. It can be triggered by an external TTL signal or internally by an adjustable signal threshold on one or multiple selected channels. A busy TTL signal can be extracted and used as a trigger for the charge readout. The digital waveform data is transmitted via an optical link to the DAQ computer.

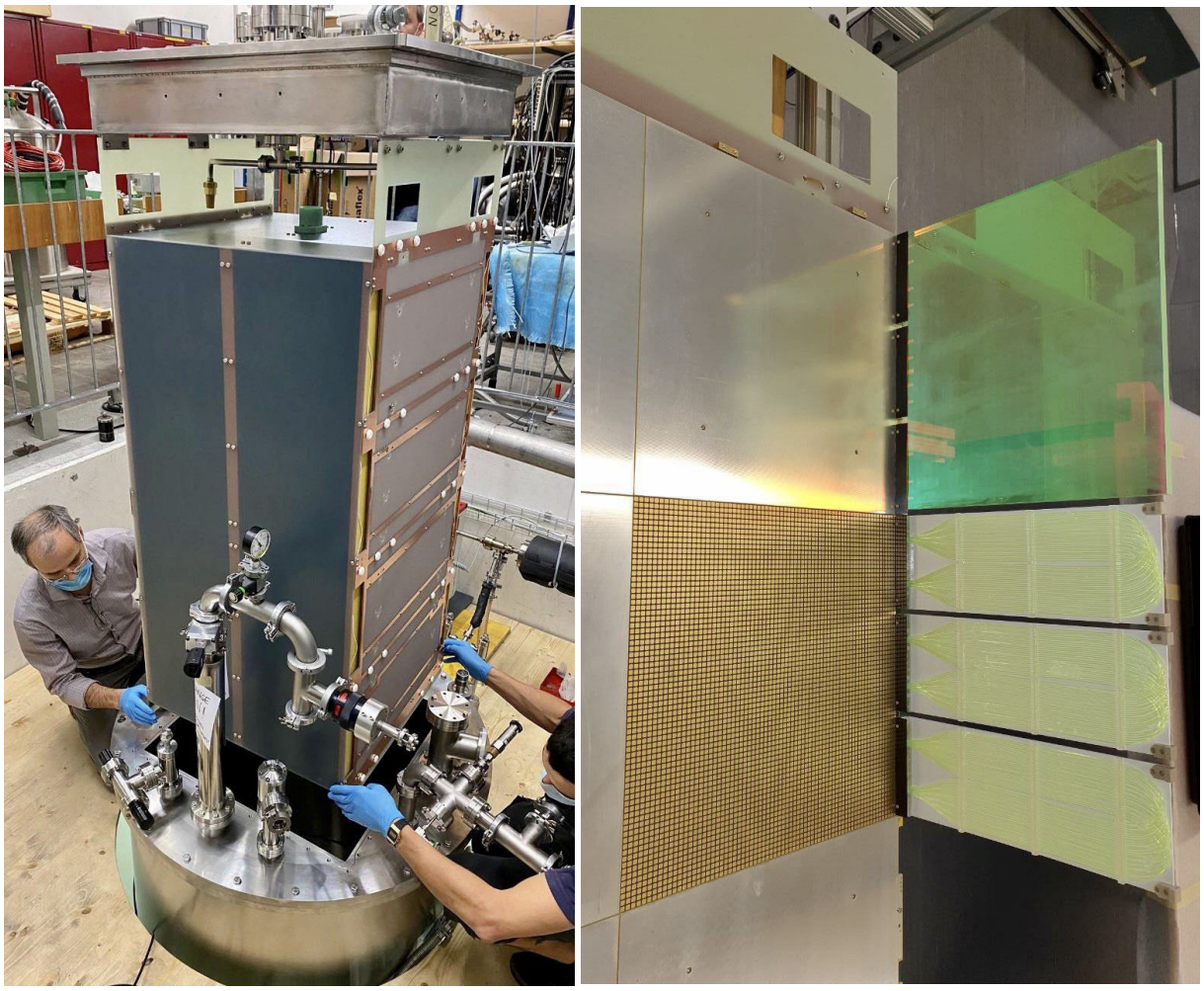

(a) **(b)**

Figure 6.7 – Module 0 HV test setup. (a) Module during insertion to the detector cryostat. The G10 module structure is mounted to a vacuum pocket below the top flange to reduce heat input. (b) Part of the module equipped with light and charge detectors. The three LCM panels are placed next to the pixel PCB. The ArCLight is mounted on top next to a dummy pixel PCB.

For each run, a separate calibration of the SiPMs was conducted. A blue LED light source was used to get high statistics and to have an adjustable light emission amplitude. The blue light can reach directly into the WLS plastic of the ArCLight, therefore it is not altered by the timing characteristics of the scintillation in LAr and neither the ones of the WLS process in TPB. One can assume that all photons of a LED pulse arrive at the same time in the WLS plastic since the time differences between in the time of travel are much smaller than the rise time of the electronics or the decay time of the WLS plastic. The measured waveform data is integrated within a certain integration window (gate). In Fig. 6.8 an example average waveform and the corresponding integral spectrum (80 ns) is shown. In the spectrum the single p.e. peaks are observable. By calculating the difference of ADC channels between two peaks, one can determine the gain and thus the number of p.e. per event.

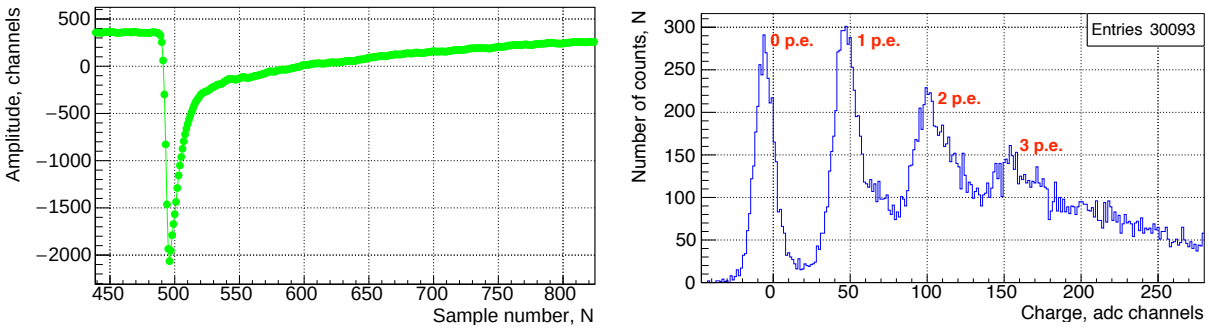

(a) (b)

Figure 6.8 – Example calibration data of a single channel over 30k events: (a) Average waveform in ADC units (1 time sample = 10 ns), (b) ADC channel integral spectrum with pedestal subtraction (no baseline subtraction) for a 80 ns time gate (sample 492-500). The observable peaks correspond to 0,1,2,3 p.e. .

To obtain the full number of p.e. generated by the LED pulse, the integration gate has to be much longer than the light pulse and the decay time of the WLS plastic (≈10 ns). However, the single p.e. peaks can only be observed for small gates (<100 ns), since for longer gates the peaks smear out and are no longer distinguishable. For longer integration gates, that include the full electronics response, only an indirect calibration can be applied. The gain obtained by a short gate has to be multiplied by the average ratio between the integral over the long gate to the one over the short gate. This indirect calibration holds as long as no late photons arrive after the short gate. For the following analysis, the initial calibration was done with a 80 ns gate and this calibration was transferred as described to a 500 ns gate. The 500 ns gate also allows measurement of late-arriving photons, but it is not yet affected by noise that dominates the signal in even longer gates >1000 ns.

6.4 Light reconstruction with track data

To obtain any information about the efficiency and resolution of the ArCLight system, the light yield induced by the particles inonising with LAr has to be reconstructed. To do this, the tracks reconstructed from the charge readout data are used.
To simplify the light reconstruction, only non-stopping cosmic-muon like tracks are considered in this analysis. Cosmic muons are the dominant interactions measured in the used setups. For each test run, events were selected by applying several cuts:

- In the first cut, only events were selected that show a good track reconstruction quality. This cut depends on the charge readout system used and therefore varies between the test runs. Here, mainly the number of recorded charge hits, number of reconstructed clusters and residual of the charge hits to the reconstructed tracks are used.

- The second cut selects only events with a single track. Multiple tracks could lead to ambiguities in the light reconstruction procedure.

- In a third cut, the length of the track is restricted. Only events that cross the whole TPC (or the whole pixel board for Mod 0) are selected to remove tracks of stopping muons and other interacting particles.
- For the Mod 0 run, an additional cut has to be applied to get only tracks that are crossing the detector vertically since the pixel board sits below the ArCLight panel (see Fig. 6.7).

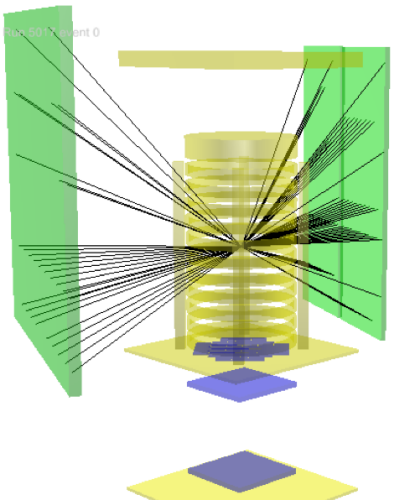

Figure 6.9 – Single step of the light reconstruction for Purity Run I algorithm based on track data. The ring shaped TPC (yellow centre), one ArCLight panel (green left), two LCM panels (green right), the muon telescope (blue) and support structures (yellow) are implemented in TGeo. For a single point on the track (here in the centre of the ring shaped TPC) the algorithm checks if the connecting line (black) to a grid point on the light detector is blocked by any structure and if not it calculates the corresponding solid angle. The total solid angles are summed up over all grid points and along the extended track.

Each detector setup was implemented in a ROOT TGeo based geometry simulation. The selected tracks are assumed to cross the entire TPC. Thus, for each event, the corresponding track was inserted to this simulation and extended to the TPC boundaries. The track was then discretised to single points with a 1 mm resolution along the track assuming an infinitely thin track. For each point, the solid angle to the light detector in the setup was calculated. The solid angle was approximated as

$$\omega = \frac{S}{d^2}\cos(\theta), \tag{6.2}$$

where S is the surface area of the detector, d the distance to the centre of the detector surface and θ the angle of incidence of the connecting line to the centre of the detector. To account for large errors of the approximation in Eq.6.2, the light detectors surfaces were divided to a grid of subsurfaces. In Purity Run I/II objects blocking the direct light yield from to a part of the detector have to be considered. If the direct connecting line between the emission point and a subsurface is blocked by any structure, this subsurface is not taken into account in the calculation of the total solid angle. The total solid angle

is the sum of the solid angle to each non-blocked subsurface. The total solid angle per point is then normalised (divided by 4π) and summed up over the whole extended track to get the normalised number of reconstructed photons $\tilde{n}_{\gamma-r}$. This procedure is depicted in Fig. 6.9. By multiplying $\tilde{n}_{\gamma-r}$ with the number of photons emitted per mm in LAr ϵ, one gets the total number of photons hitting the light detector surface within the considered event. ϵ depends on the dE/dx of the interacting particle and the electric field.

In this light reconstruction, Rayleigh scattering is neglected as for all setups (except Mod 0) the optical path between the measured tracks and the light detectors is much smaller than the Rayleigh scattering length. For the Mod 0 setup this does not hold strongly (TPC height: 120 cm) however, the contribution to the total solid angles of emission points at larger distances is negligible.

6.5 Photon detection efficiency results

To quantify the impact of the design changes on the detector performance the PDE of the different versions can be compared. In this section, the impact of the mirror foil and the TPB coating technique are studied. The PDE of the ArCLight system can be calculated by comparing the number of true measured photons and the number of photons that hit the ArCLight as obtained from the measured particle tracks. Therefore, the track events have to be matched to the corresponding light event. This synchronisation is not trivial since, in all the considered runs, the charge and light readout were running with separate unsynchronised clocks and had missing events due to too high event rates. Thus, the efficiency of this event synchronisation is below unity. By matching the time differences between the recorded events of the two systems in each run over 95 % of the track events could be matched to a light event.

Since the light can only be measured for a limited gate length (see 6.3), not the full scintillation light can be detected. As described in Chapter 3, the LAr scintillation process has a slow and fast time component. If a certain gate length T_g on the light readout is chosen, due to the slow component ($\tau_S \approx 1.5\,\mu s$), late photons are not detected. However, in this light reconstruction, no timing information is considered and only the total number of photons hitting the detector is calculated. To account for this, a correction factor has to be applied. The number of late photons is calculated by calculating the time-dependent detector response for a muon interaction. The pure detector response has to be folded with the timing characteristics of the LAr scintillation process. In the waveform obtained from the LED calibration runs, the pure detector response $I_{det}(t)$ is measured (except TPB WLS), since all photons are assumed to arrive at the same time on the detector (see Sec. 6.3). The timing characteristics of the LAr scintillation $I_{scint}(t)$ are modelled following Whittington, Mufson, and Howard [85], where also the TPB WLS process is folded in. By normalising $I_{det}(t)$ and calculating the convolution with $I_{scint}(t)$, one gets the full detector response for a muon interaction that would be expected for an infinite

readout gate. Thus, the gate acceptance ξ can be calculated as

$$\xi\left(T_g\right) = \frac{\int_{t=0}^{T_g} (I_{det} * I_{scint})(t)\mathrm{d}t}{\int_{t=0}^{\infty} (I_{det} * I_{scint})(t)\mathrm{d}t}. \tag{6.3}$$

The PDE of the ArCLight η for a single event can now be calculated as

$$\eta = \frac{n_{\gamma-m}}{\xi\epsilon\tilde{n}_{\gamma-r}}, \tag{6.4}$$

where $n_{\gamma-m}$ is the total number of measured photons within the event.
The goal for PurityRun I and II was to compare the ArCLight versions with and without mirror foil. In both of these runs, the drift field was created by a field shaping rings. This led to a much lower field uniformity than in the SingleCube or Mod 0. Thus, ϵ could not be determined absolutely, since it is field dependent. However, an upper limit for ϵ can be obtained by taking its value at zero field conditions. Therefore a lower limit on the PDE can be determined. Since the field is the same for both tested ArCLight versions in this run, the ratio between these lower PDE limits is the same as the ratio between their absolute PDEs and the upper limits can still be used to compare the two. At zero field, the average energy required to produce a single photon W_{ph-max} for a MIP is $(24.4 \pm 1.7)\,\mathrm{eV}$ [51]. Cosmic muons can be approximated as MIPs. For an average ionisation energy loss $\mathrm{d}E/\mathrm{d}x = 2.1\,\mathrm{MeV/cm}$ of a cosmic muon, the number of produced photons per mm is

$$\epsilon_{max} = \frac{\frac{\mathrm{d}E}{\mathrm{d}x}}{W_{ph-max}} = (8.61 \pm 0.59) \times 10^3\,\mathrm{mm}^{-1}. \tag{6.5}$$

And with a gate length T_g set to 500 ns, the gate acceptance ξ is $(16.06 \pm 0.52)\,\%$.
In course of the PurityRun II, large parts of the mirror foil detached from the ArCLight panel that was initially covered with it. Since it could not be determined when this detachment happened, the data from this panel can not be considered for the comparison analysis. To compare the PDE of the ArCLight versions with and without mirror foil the data from PurityRun I and II are taken into account. Both of the compared panels were TPB coated by airbrush. The results for the lower PDE limit can be seen in Fig. 6.10. The mean PDE limits for the versions with and without mirror foil are $\eta_{wM-ab} \geq (0.0887 \pm 0.0068)\,\%$ and $\eta_{woM-ab} \geq (0.0757 \pm 0.0058)\,\%$ respectively.
In the SingleCube run, the new field-shaping structure enabled a much better uniformity of the field compared to the PurityRuns. Thus, an absolute value for ϵ could be determined and an estimation of the absolute PDE could be worked out. As described in Sec. 3.2, the total scintillation light yield gets attenuated in the presence of an electric field. At the nominal field of $500\,\mathrm{V\,cm}^{-1}$ the light attenuation factor for cosmic muons is $q(500\,\mathrm{V\,cm}^{-1}) = 0.802 \pm 0.086$ [86]. Thus, the average energy needed to produce a single photon is

$$W_{ph}(E = 500\,\mathrm{V\,cm}^{-1}) = \frac{W_{ph-max}}{q(E)} = (30.4 \pm 3.4)\,\mathrm{eV}. \tag{6.6}$$

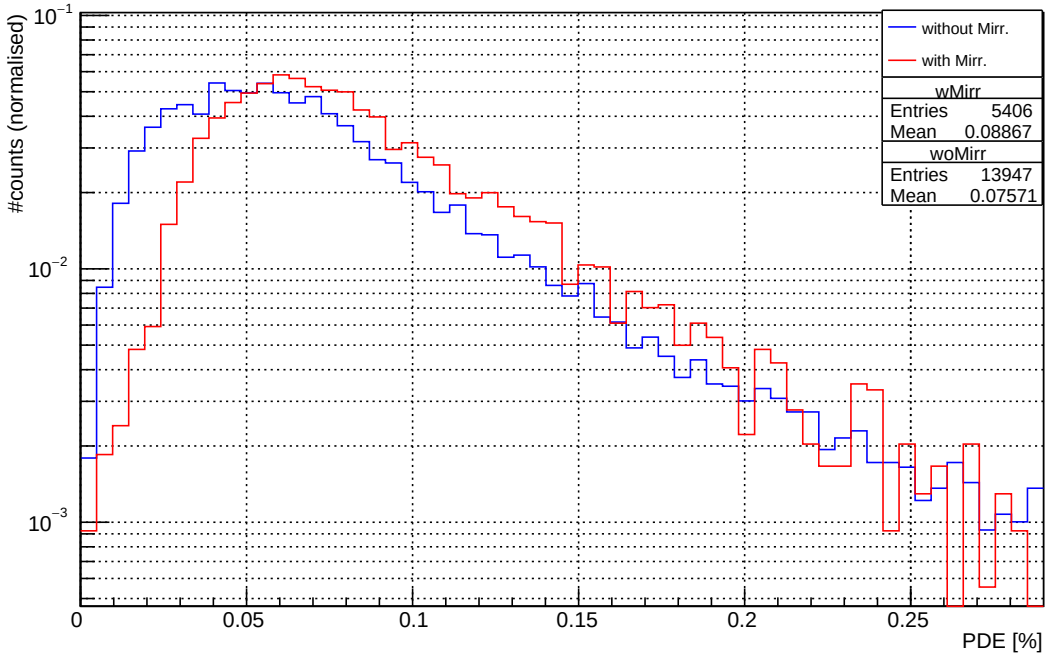

Figure 6.10 – Impact of the mirror foil on the overall PDE. The PDE for the versions without and with were measured in PurityRun II and I respectively.

And therefore, the number of photons emitted per mm for a MIP is

$$\epsilon(E = 500\,\mathrm{V\,cm^{-1}}) = \frac{\frac{\mathrm{d}E}{\mathrm{d}x}}{W_{ph}(E)} = (6.84 \pm 0.77) \times 10^3\,\mathrm{mm^{-1}}. \tag{6.7}$$

In Fig. 6.11 the combined results on the overall PDE from the SingleCube and Mod 0 run are shown. The overall PDE for the version with airbrush coating and evaporation coating is $\eta_{woM-ab} = (0.1020 \pm 0.0035)\,\%$ and $\eta_{woM-evap} = (0.2055 \pm 0.0070)\,\%$ respectively. The evaporation coating panel has an overall PDE which is by a factor 2.015 ± 0.069 larger compared to the airbrush coated panel. It has to be taken into account that the evaporation coated panel was also equipped with an additional dichroic mirror on the backside surface. However, the impact of the mirror foil is of minor significance as shown above. Thus, the increase of the PDE can be attributed to the improved TPB coating.

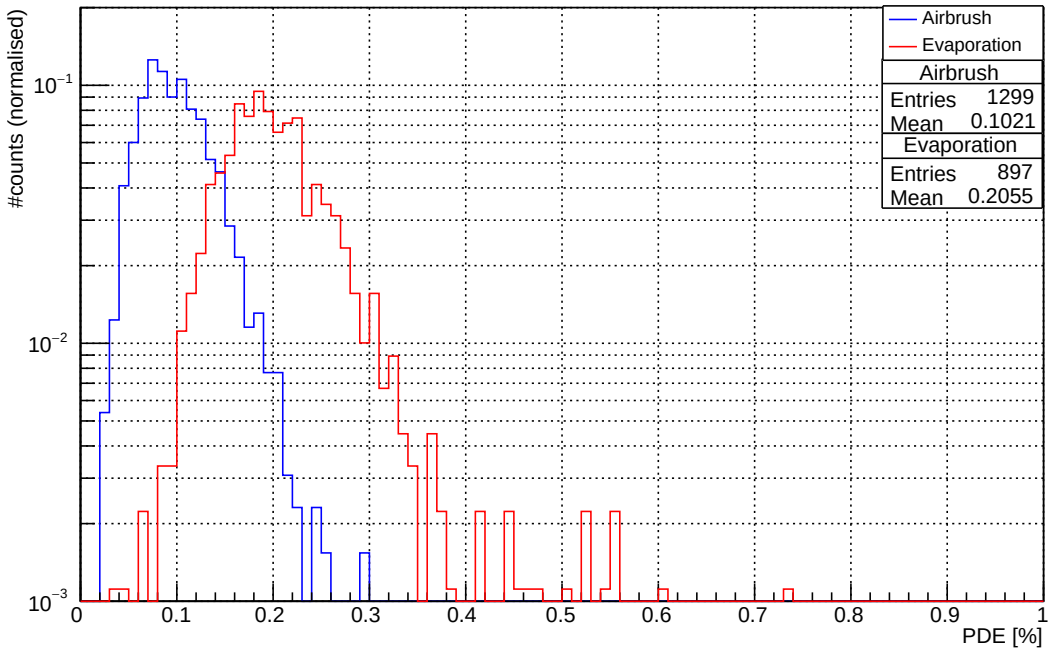

Figure 6.11 – Impact of the TPB coating technique on the overall PDE. The PDE for the ArCLight versions with airbrush coating and evaporation coating were measured in the SingleCube run and the Mod 0 run respectively.

6.6 Spatial resolution results

The methods established with the optical simulation for the reconstruction of the photon emission point were also applied to the real data of the SingleCube run.
For the direction along the different SiPM positions, here called y (see 6.6b), a straight forward approach is chosen. In a single event, the number of p.e. measured in each SiPM is assigned to the position of this SiPM. As established in the optical simulation, the centre of the distribution of these hit positions $\tilde{y}_{meas}$ is then taken as an estimator for the y_{true}. Unlike in the simulation, in the real data from SingleCube, the photons are not emitted in a single point but along a track. Thus, the centre of gravity of the track is considered as y_{true}. This is only a reasonable choice for tracks with a low inclination in y direction and thus only tracks with $\theta < 0.5$ are chosen. In order to approach a 1 to 1 correlation between y_{true} and y_{meas}, $\tilde{y}_{meas}$ has to be scaled by constant factor as previously done in the simulation. This factor is calculated by taking a linear fit of $\tilde{y}_{meas}$ vs. y_{true}. The resulting correlation is shown in Fig. 6.12. Based on this 2D distribution the RMSE is calculated for each y_{true} bin to get the y dependent spatial resolution. In Fig. 6.13 the systematic offset (mean of δy) and the y resolution (RMSE of δy) are shown. The algorithm fails in the region close to the edges (y>100 mm or y< − 100 mm). For the inner part of the detector ($-100\,\text{mm} < y < 100\,\text{mm}$), the average resolution is $(53.6 \pm 1.9)\,\text{mm}$.
As before in the optical simulation, any attempts for a conservative reconstruction failed for the z direction. Reconstruction attempts also failed for the x direction (away from the ArCLight).

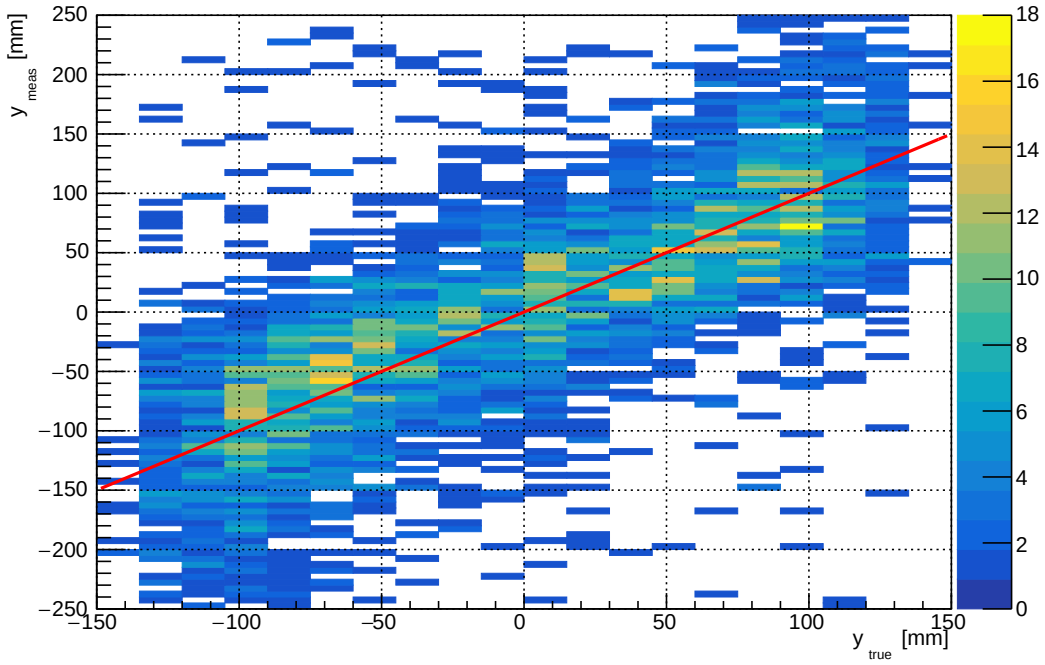

Figure 6.12 – 2D histogram of y_{meas} vs. y_{true} for the SingleCube run. The approached 1 to 1 correlation is depicted by the red line.

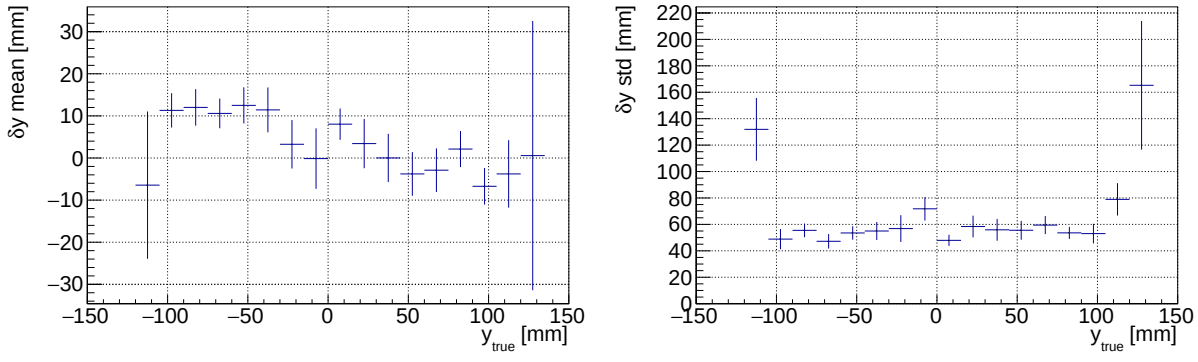

(a) **(b)**

Figure 6.13 – Systematic offset (a) and spatial resolution (b) of the y coordinate reconstruction in SingleCube data.

6.7 Energy threshold for neutron detection

As described in Sec. 4.4, detached energy deposits due to neutron-induced recoils can only be distinguished from other interactions using the light readout. The measurement of the PDE, $\eta_{ArCLight}$, enables one to set a threshold on the minimum neutron energy required to allow an efficient tagging.
The minimum energy of an ionising particle that can be detected by ArCLight is

$$E_{th} \simeq \frac{n_{\gamma,min}}{\eta_{ArCLight}} \cdot \frac{1}{R_{\gamma}(LAr)} \cdot \frac{4\pi}{\theta_{min}}, \tag{6.8}$$

where $n_{\gamma,min}$ is the minimum number of p.e. to overcome the ArCLight dark-noise level, $R_{\gamma}(LAr)$ is the average photon yield in LAr per unit of deposited energy and θ_{min} is the minimum solid angle of any point in the detector to the light detector. The last factor corrects for the fact that not all emitted photons hit the sensitive surface of the light detectors. By taking the minimum light yield of a particle at nominal field, namely for a MIP, $R_{\gamma,max} = (4.10 \pm 0.29) \times 10^4\,\mathrm{MeV}^{-1}$ [51] an upper limit of the threshold for any ionising particle can be set. A conservative estimate for $n_{\gamma,min}$ is 3 p.e. that can be achieved with a relatively high light trigger threshold. The minimum solid angle θ_{min} for the ArgonCube ND design is 0.351 sr. With the PDE $(0.2055 \pm 0.0070)\,\%$ of the ArCLight without mirror foil and evaporated TPB coating, one gets a upper limit on the threshold of $E_{th,max} = (12.7 \pm 4.4)\,\mathrm{MeV}$. This value does not consider any gate acceptance of the light readout and just account for the pure PDE (assuming an infinite integration gate). Thus, if one applies a discrete gate, the threshold energy has to be

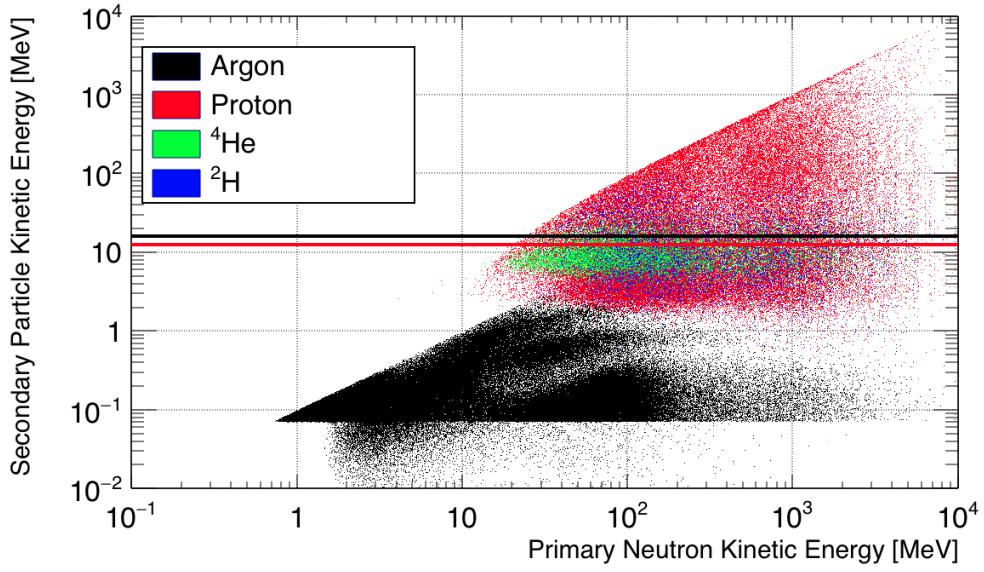

Figure 6.14 – Kinetic energy distribution of secondary particles after a neutron interaction depending on the energy of the initial neutron. In total 100k neutrino interactions are simulated by GEANT4 based MC simulations. The red line indicates the energy threshold for light detection by ArCLight. The black line indicates the energy threshold for recoiled protons to be measured as a track.

divided by the corresponding gate acceptance factor. For the neutron tagging the gate has to be shorter than the time difference between two neutrino events ($\sim 100\,\mathrm{ns}$ [71]). This threshold energy can be used to set a threshold for tagging fast-neutrons-induced recoils. In Fig. 6.14 the kinetic energy distribution of secondary particles after a fast-neutron interaction (based on MC simulations) are shown with the calculated threshold for light detection with ArCLight. It is assumed that the full kinetic energy is deposited in the detector. The scintillation yield per deposited energy for non-relativistic protons is approximately the same as for a MIP [51]. Thus, the energy threshold calculated for MIPs holds also for protons. Only tracks longer than 3 mm can be deduced as a track by the charge readout system. As shown in the same figure, the energy needed to overcome this limit by the charge readout is larger than the minimum energy detectable by ArCLight. To tag a fast neutron the spatial and timing resolution of the detector-wide light detection system has to be good enough to associate a recoil proton with the corresponding neutrino event. The minimum distance between a recoil proton and any other energy deposit is 30 cm [71]. This spatial resolution requirement on ArCLight is already achieved with the conservative methods used in this thesis (see Fig. 6.13). The mean time separation between two neutrino-events is expected to be 280 ns for the DUNE ND design. The timing resolution of ArCLight is to be determined yet but following the timing characteristics of the different system parts (see Sec. 5), it is expected to be much higher than required for the neutron tagging.

Chapter 7

Conclusion and Outlook

In this thesis, I have proved that the ArCLight light detection system fulfils the requirements for the DUNE ND. In course of this prototyping work, two major design changes were realised. In order to make the structure applicable at cryogenic temperatures, I removed the mirror foil that was initially used to improve efficiency of the light trapping. By removing this mirror foil the robustness of ArCLight, in particular during cool-down and warm-up processes, was significantly improved. The risk of delamination of the foil or induced shear stress leading to potential cracking of the structure was eliminated. The second change was the implementation of a new coating technique of the WLS TPB layer. The airbrush coating was replaced with a vacuum-evaporation coating, for which I designed and successfully operated an evaporation chamber. The evaporated coating has led to a considerable improvement in the uniformity of the TPB layer. During several prototyping test runs performed by the ArgonCube collaboration, the ArCLight structure could be tested multiple times. This allowed analysing the impact of the design changes on the performance of ArCLight. Removing the mirror foil has led to a drop of the overall PDE by $\approx 15\,\%$. This is compensated by the improved TPB coating which has led to the increase of the PDE by a factor 2.015 ± 0.069. For the final version of ArCLight, I measured an overall PDE of $(0.2055 \pm 0.0070)\,\%$.

In order to establish an optical simulation of the ArgonCube detector, I contributed to the implementation of the optical parameters to a GEANT4 based simulation of ArCLight. I used this simulation to establish an algorithm to reconstruct the coordinate perpendicular to the charge drift direction of the light emission point. This algorithm was then applied to experimental data to establish a first estimate for the spatial resolution of ArCLight in one coordinate. Due to the fact that only a single panel was tested (In the final design there will be neighbouring panels), the algorithm failed for light emissions close to the edge of the panel. For the middle part of the panel, an average spatial resolution of $(53.6 \pm 1.9)\,\mathrm{mm}$ could be measured. Further, I used the simulation to get an estimate for the PDE and the impact that the design changes had on it. The PDE in the simulation is generally overestimated. This issue was also reported in different applications of the optical simulation and will be fixed for future usage of it.

I can confirm that the ArCLight system fulfils the PDE and spatial resolution requirements for the DUNE ND. In particular, I could deduce an energy threshold to detect charged particles by scintillation light. This threshold is lower than the energy needed for the charge readout to detect a passing particle as a track. Hence, every fast-neutron-

induced proton recoil that is detected by the charge readout can be identified by the light readout and be tagged due to the fast timing resolution.
The next steps towards the DUNE ND concerning ArCLight will be the production of further test of multiple panels in a full ArgonCube module, and later for multiple modules in the 2x2 demonstrator. The 2x2 demonstrator will be used to continue the characterisation of the ArCLight performance and to test its integration into the detector system. In order to improve spatial resolution, better light reconstruction algorithms have to be developed, potentially with the integration of AI methods. Furthermore, the spatial reconstruction can be improved by combining the data from multiple ArCLight panels and data acquired by LCM panels. After the completion of the prototyping campaign with the ArgonCube 2x2 demonstrator, the ND design will be finalised and implemented.

Acknowledgements

First of all, I would like to thank my supervisor Prof. Igor Kreslo for giving me the opportunity to do this thesis. It was always very inspiring to work with you and see your enthusiasm for research. Whenever I was stuck with something I could be sure you had a solution for it.
A special thanks goes to Dr. James Sinclair who supported me especially during the writing of this thesis. You always had an open ear for my questions and showed a great patience in teaching me your knowledge on neutrino research.
Further, I would like to thank Dr. Francesco Piastra who guided me through most of my lab work. I really enjoyed the days (and nights) with you in the lab with all the good music.
Many thanks go to Roman Berner and Patrick Koller for supporting me through my whole thesis work. The discussions with you helped me to solve all the problems I encountered. Also I would like to acknowledge Patrick for providing his fast neutron recoil studies that built the basis for Section 6.7 and Roman for contributing to the construction of the evaporation chamber.
I would like to thank the members of the LHEP workshop Roger Hänni, Jan Christen, Lorenzo Meier, Lino Risch and Camilla Tognina for solving all the mechanical and electronic problems that I encountered and teaching me valuable skills.
Furthermore, I would like to thank also everybody else at LHEP for making this year full of lasting memories.
Last but not least I wish to thank my friends and family for always being there for me and enduring me in stressful times.

Bibliography

[1] J. Chadwick. "Intensitätsverteilung im magnetischen Spectrum der β-Strahlen von radium B + C". In: *Verhandl. Dtsc. Phys. Ges.* Vol. 16. 1914, p. 383. URL: https://cds.cern.ch/record/262756.

[2] W. Pauli. "Letter of the 4th December 1930". In: *Pauli Archive at CERN* (1930).

[3] J. Chadwick. "Possible Existence of a Neutron". In: *Nature* 129 (1932), p. 312. DOI: 10.1038/129312a0.

[4] E. Fermi. "Tentativo di una teoria dei raggi β". In: *Il Nuovo Cimento (1924-1942)* 11.1 (1934), p. 1.

[5] H. Bethe and R. Peierls. "The 'neutrino'". In: *Nature* 133 (1934), p. 532. DOI: 10.1038/133532a0.

[6] C. L. Cowan et al. "Detection of the Free Neutrino: a Confirmation". In: *Science* 124.3212 (1956), pp. 103–104. ISSN: 0036-8075. DOI: 10.1126/science.124.3212.103. eprint: https://science.sciencemag.org/content/124/3212/103.full.pdf. URL: https://science.sciencemag.org/content/124/3212/103.

[7] C. S. Wu et al. "Experimental Test of Parity Conservation in Beta Decay". In: *Physical Review* 105.4 (Feb. 1957), pp. 1413–1415. ISSN: 0031-899X. DOI: 10.1103/PhysRev.105.1413. URL: https://link.aps.org/doi/10.1103/PhysRev.105.1413.

[8] G. Danby et al. "Observation of High-Energy Neutrino Reactions and the Existence of Two Kinds of Neutrinos". In: *Physical Review Letters* 9.1 (July 1962), pp. 36–44. ISSN: 0031-9007. DOI: 10.1103/PhysRevLett.9.36. URL: https://link.aps.org/doi/10.1103/PhysRevLett.9.36.

[9] A. D. Sakahrov. "Violation of CP in variance, C asymmetry, and baryon asymmetry of the universe". In: *JETP Lett* 5 (1967), pp. 24–27. DOI: 10.1070/pu1991v034n05abeh002497.

[10] M. B. Gavela et al. "Standard model CP violation and baryon asymmetry". In: *Mod. Phys. Lett. A* 9 (1994), pp. 795–810. DOI: 10.1142/S0217732394000629. arXiv: hep-ph/9312215.

[11] R. Davis, D. S. Harmer, and K. C. Hoffman. "Search for Neutrinos from the Sun". In: *Physical Review Letters* 20.21 (May 1968), pp. 1205–1209. ISSN: 0031-9007. DOI: 10.1103/PhysRevLett.20.1205. URL: https://link.aps.org/doi/10.1103/PhysRevLett.20.1205.

[12] J. Bahcall et al. "Solar neutrino flux". In: *Astrophys. J.* 137 (1963), pp. 344–346. DOI: 10.1086/147513.

[13] J. Bahcall. “The solar neutrino problem”. In: *Comments Nucl. Part. Phys.* 5.2 (1972), pp. 59–64.

[14] J. N. Bahcall and R. Davis. “Solar Neutrinos - a Scientific Puzzle”. In: *Science* 191 (1976), pp. 264–267. DOI: 10.1126/science.191.4224.264.

[15] B. Pontecorvo. “Neutrino experiments and the problem of conservation of leptonic charge”. In: *Sov. Phys. JETP* 26.984-988 (1968), p. 165.

[16] M. L. Perl et al. “Evidence for Anomalous Lepton Production in positron-electron Annihilation”. In: *Phys. Rev. Lett.* 35 (22 Dec. 1975), pp. 1489–1492. DOI: 10.1103/PhysRevLett.35.1489.

[17] M. L. Perl et al. “Properties of the proposed τ charged lepton”. In: *Physics Letters B* 70.4 (1977), pp. 487–490.

[18] K. Hirata et al. “Experimental study of the atmospheric neutrino flux”. In: *Physics Letters B* 205.2-3 (1988), pp. 416–420.

[19] D. Casper et al. “Measurement of atmospheric neutrino composition with the IMB-3 detector”. In: *Phys. Rev. Lett.* 66 (20 May 1991), pp. 2561–2564. DOI: 10.1103/PhysRevLett.66.2561. URL: https://link.aps.org/doi/10.1103/PhysRevLett.66.2561.

[20] P. A. Cherenkov. “Visible emission of clean liquids by action of gamma radiation”. In: *Dokl. Akad. Nauk SSSR.* Vol. 2. 8. 1934, pp. 451–454.

[21] B. Adeva et al. “Measurement of Z0 decays to hadrons, and a precise determination of the number of neutrino species”. In: *Physics Letters B* 237.1 (1990), pp. 136–146.

[22] Y. Fukuda et al. “Measurement of a small atmospheric $\nu\mu/\nu$e ratio”. In: *Physics Letters, Section B: Nuclear, Elementary Particle and High-Energy Physics* 433.1-2 (Aug. 1998), pp. 9–18. ISSN: 03702693. DOI: 10.1016/S0370-2693(98)00476-6.

[23] K. Kodama et al. “Observation of tau neutrino interactions”. In: *Physics Letters, Section B: Nuclear, Elementary Particle and High-Energy Physics* 504.3 (Apr. 2001), pp. 218–224. ISSN: 03702693. DOI: 10.1016/S0370-2693(01)00307-0.

[24] Q. R. Ahmad et al. “Direct Evidence for Neutrino Flavor Transformation from Neutral-Current Interactions in the Sudbury Neutrino Observatory”. In: *Physical Review Letters* 89.1 (June 2002), p. 011301. ISSN: 0031-9007. DOI: 10.1103/PhysRevLett.89.011301. URL: https://link.aps.org/doi/10.1103/PhysRevLett.89.011301.

[25] F. An et al. “Observation of electron-antineutrino disappearance at Daya Bay”. In: *Physical Review Letters* 108.17 (2012), p. 171803.

[26] K. Abe et al. “Observation of Electron Neutrino Appearance in a Muon Neutrino Beam”. In: *Phys. Rev. Lett.* 112 (2014), p. 061802. DOI: 10.1103/PhysRevLett.112.061802. arXiv: 1311.4750 [hep-ex].

[27] A. Bettini. *Introduction to Elementary Particle Physics*. Cambridge University Press, 2008. ISBN: 9781139472555.

[28] Z. Maki, M. Nakagawa, and S. Sakata. *Remarks on the Unified Model · of Elementary Particles*. Tech. rep. 5. 1962. URL: https://academic.oup.com/ptp/article/28/5/870/1858382.

[29] P. A. Zyla et al. "Review of particle physics". In: *Progress of Theoretical and Experimental Physics* 2020.8 (2020), pp. 1–2093. ISSN: 20503911. DOI: 10.1093/ptep/ptaa104. URL: https://doi.org/10.1093/ptep/ptaa104.

[30] L. Wolfenstein. "Neutrino oscillations in matter". In: *Physical Review D* 17.9 (May 1978), pp. 2369–2374. ISSN: 0556-2821. DOI: 10.1103/PhysRevD.17.2369. URL: https://link.aps.org/doi/10.1103/PhysRevD.17.2369.

[31] I. Esteban et al. "The fate of hints: updated global analysis of three-flavor neutrino oscillations". In: *JHEP* 09 (2020), p. 178. DOI: 10.1007/JHEP09(2020)178. arXiv: 2007.14792 [hep-ph].

[32] K. Abe et al. *Hyper-Kamiokande Design Report*. 2018. arXiv: 1805.04163 [physics.ins-det].

[33] R. Acciarri et al. *Long-Baseline Neutrino Facility (LBNF) and Deep Underground Neutrino Experiment (DUNE) Conceptual Design Report Volume 2: The Physics Program for DUNE at LBNF*. Dec. 2015. URL: http://arxiv.org/abs/1512.06148.

[34] B. Abi et al. "Volume I. Introduction to DUNE". In: *Journal of Instrumentation* 15.08 (Aug. 2020), T08008–T08008. DOI: 10.1088/1748-0221/15/08/t08008.

[35] B. Abi et al. "Volume III. DUNE far detector technical coordination". In: *Journal of Instrumentation* 15.08 (Aug. 2020), T08009–T08009. DOI: 10.1088/1748-0221/15/08/t08009.

[36] B. Abi et al. "Volume IV. The DUNE far detector single-phase technology". In: *Journal of Instrumentation* 15.08 (Aug. 2020), T08010–T08010. DOI: 10.1088/1748-0221/15/08/t08010.

[37] B. Abi et al. "Long-baseline neutrino oscillation physics potential of the DUNE experiment: DUNE Collaboration". In: *European Physical Journal C* 80.10 (Oct. 2020). ISSN: 14346052. DOI: 10.1140/epjc/s10052-020-08456-z.

[38] R. Berner et al. "First Operation of a Resistive Shell Liquid Argon Time Projection Chamber: A New Approach to Electric-Field Shaping". In: *Instruments* 3.2 (May 2019), p. 28. ISSN: 2410-390X. DOI: 10.3390/instruments3020028. URL: https://www.mdpi.com/2410-390X/3/2/28.

[39] D. R. Nygren. "The time projection chamber: A new 4 pi detector for charged particles, eConf". In: *C740805* 58 (1974).

[40] C. Rubbia. *The liquid-argon time projection chamber: a new concept for neutrino detectors*. Tech. rep. CERN-EP-INT-77-8. Geneva: CERN, 1977. URL: https://cds.cern.ch/record/117852.

[41] C. Allen and C. Allen. *Astrophysical Quantities*. Springer series in electrophysics. Athlone Press, 1973. ISBN: 9780485111507.

[42] C. Tegeler, R. Span, and W. Wagner. "A new equation of state for argon covering the fluid region for temperatures from the melting line to 700 K at pressures up to 1000 MPa". In: *Journal of Physical and Chemical Reference Data* 28.3 (1999), pp. 779–850.

[43] C. Amsler et al. "Review of Particle Physics". In: *Phys. Lett. B* 667 (2008), pp. 1–1340. DOI: 10.1016/j.physletb.2008.07.018.

[44] E. Shibamura et al. “Drift velocities of electrons, saturation characteristics of ionization and W-values for conversion electrons in liquid argon, liquid argon-gas mixtures and liquid xenon”. In: *Nucl. Instrum. Meth.* 131 (1975), pp. 249–258. DOI: 10.1016/0029-554X(75)90327-4.

[45] M. Miyajima et al. “Average energy expended per ion pair in liquid argon”. In: *Phys. Rev. A* 9 (1974), pp. 1438–1443. DOI: 10.1103/PhysRevA.9.1438.

[46] A. Gonidec et al. *Temperature and Electric Field Strength Dependence of Electron Drift Velocity in Liquid Argon*. Tech. rep. ATL-LARG-96-058. ATL-A-PN-58. Geneva: CERN, Dec. 1996. URL: https://cds.cern.ch/record/682073.

[47] W. Walkowiak. “Drift velocity of free electrons in liquid argon”. In: *Nucl. Instrum. Meth. A* 449 (2000), pp. 288–294. DOI: 10.1016/S0168-9002(99)01301-7.

[48] S. Amoruso et al. “Analysis of the liquid argon purity in the ICARUS T600 TPC”. In: *Nucl. Instrum. Meth. A* 516 (2004), pp. 68–79. DOI: 10.1016/j.nima.2003.07.043.

[49] E. Aprile, K. Giboni, and C. Rubbia. “A Study of Ionization Electrons Drifting Large Distances in Liquid and Solid Argon”. In: *Nucl. Instrum. Meth. A* 241 (1985), pp. 62–71. DOI: 10.1016/0168-9002(85)90516-9.

[50] M. Boulay and A. Hime. “Technique for direct detection of weakly interacting massive particles using scintillation time discrimination in liquid argon”. In: *Astropart. Phys.* 25 (2006), pp. 179–182. DOI: 10.1016/j.astropartphys.2005.12.009.

[51] T. Doke et al. “Absolute Scintillation Yields in Liquid Argon and Xenon for Various Particles”. In: *Japanese Journal of Applied Physics* 41.Part 1, No. 3A (Mar. 2002), pp. 1538–1545. ISSN: 0021-4922. DOI: 10.1143/JJAP.41.1538. URL: https://iopscience.iop.org/article/10.1143/JJAP.41.1538.

[52] E. Grace and J. A. Nikkel. “Index of refraction, Rayleigh scattering length, and Sellmeier coefficients in solid and liquid argon and xenon”. In: *Nucl. Instrum. Meth. A* 867 (2017), pp. 204–208. DOI: 10.1016/j.nima.2017.06.031. arXiv: 1502.04213 [physics.ins-det].

[53] G. Seidel, R. Lanou, and W. Yao. “Rayleigh scattering in rare gas liquids”. In: *Nucl. Instrum. Meth. A* 489 (2002), pp. 189–194. DOI: 10.1016/S0168-9002(02)00890-2. arXiv: hep-ex/0111054.

[54] N. Ishida et al. “Attenuation length measurements of scintillation light in liquid rare gases and their mixtures using an improved reflection suppresser”. In: *Nuclear Instruments and Methods in Physics Research Section A: Accelerators, Spectrometers, Detectors and Associated Equipment* 384.2-3 (1997), pp. 380–386.

[55] M. Sneep and W. Ubachs. “Direct measurement of the Rayleigh scattering cross section in various gases”. In: *Journal of Quantitative Spectroscopy and Radiative Transfer* 92.3 (2005), pp. 293–310.

[56] P. Cennini et al. “Performance of a three-ton liquid argon time projection chamber”. In: *Nuclear Instruments and Methods in Physics Research Section A: Accelerators, Spectrometers, Detectors and Associated Equipment* 345.2 (1994), pp. 230–243.

[57] V. Atrazhev and I. Timoshkin. "Transport of electrons in atomic liquids in high electric fields". In: *IEEE transactions on dielectrics and electrical insulation* 5.3 (1998), pp. 450–457.

[58] E. Shibamura et al. "Ratio of diffusion coefficient to mobility for electrons in liquid argon". In: *Phys. Rev. A* 20.6 (1979), p. 2547. DOI: 10.1103/PhysRevA.20.2547.

[59] J. Thomas and D. A. Imel. *Recombination of electron-ion pairs in liquid argon and liquid xenon*. Tech. rep. 2. 1987.

[60] P. Sorensen. "Anisotropic diffusion of electrons in liquid xenon with application to improving the sensitivity of direct dark matter searches". In: *Nucl. Instrum. Meth. A* 635 (2011), pp. 41–43. DOI: 10.1016/j.nima.2011.01.089. arXiv: 1102.2865 [astro-ph.IM].

[61] A. Hitachi et al. *Effect of ionization density on the time dependence of luminescence from liquid argon and xenon*. Tech. rep. 1983.

[62] S. Kubota, M. Hishida, and M. Suzuki. "Dynamical behavior of free electrons in the recombination process in liquid argon, krypton, and xenon". In: *Phys. Rev. B* 20.8 (1979), p. 3486. DOI: 10.1103/PhysRevB.20.3486.

[63] A. Wright. *Optical Attenuation in Liquid Argon*. Tech. rep. 2011.

[64] O. Palamara. "Event reconstruction in LAr-TPC". In: *AIP Conference Proceedings*. Vol. 1222. 2010, pp. 122–126. ISBN: 9780735407633. DOI: 10.1063/1.3399272. URL: https://doi.org/10.1063/1.3399272.

[65] J. Strait et al. *Long-Baseline Neutrino Facility (LBNF) and Deep Underground Neutrino Experiment (DUNE) Conceptual Design Report Volume 3: Long-Baseline Neutrino Facility for DUNE*. Jan. 2016. URL: http://arxiv.org/abs/1601.05823.

[66] B. Abi et al. "First results on ProtoDUNE-SP liquid argon time projection chamber performance from a beam test at the CERN Neutrino Platform". In: *Journal of Instrumentation* 15.12 (Dec. 2020), P12004–P12004. ISSN: 1748-0221. DOI: 10.1088/1748-0221/15/12/P12004. URL: https://iopscience.iop.org/article/10.1088/1748-0221/15/12/P12004.

[67] D. Goeldi. "A Novel Liquid Argon Time Projection Chamber Detector: The ArgonCube Concept". PhD thesis. University of Bern, 2018. URL: https://jinst.sissa.it/jinst/theses/2018_JINST_TH_002.pdf.

[68] J. Asaadi et al. "First Demonstration of a Pixelated Charge Readout for Single-Phase Liquid Argon Time Projection Chambers". In: *Instruments* 4.1 (2020), p. 9. DOI: 10.3390/instruments4010009. arXiv: 1801.08884 [physics.ins-det].

[69] D. A. Dwyer et al. "LArPix: Demonstration of low-power 3D pixelated charge readout for liquid argon time projection chambers". In: *Journal of Instrumentation* 13.10 (2018). ISSN: 17480221. DOI: 10.1088/1748-0221/13/10/P10007. URL: https://doi.org/10.1088/1748-0221/13/10/P10007.

[70] D. Nygren and Y. Mei. *Q-Pix: Pixel-scale Signal Capture for Kiloton Liquid Argon TPC Detectors: Time-to-Charge Waveform Capture, Local Clocks, Dynamic Networks*. Sept. 2018. arXiv: 1809.10213 [physics.ins-det].

[71] P. Koller. *Light Readout for Neutron Tagging in DUNE Near-Detector*. DUNE document 9525v2. DUNE, 2018.

[72] N. Anfimov et al. "Development of the Light Collection Module for the Liquid Argon Time Projection Chamber (LArTPC)". In: *Journal of Instrumentation*. Vol. 15. 7. 2020. DOI: 10.1088/1748-0221/15/07/C07022. URL: https://doi.org/10.1088/1748-0221/15/07/C07022.

[73] M. Auger et al. "ArCLight—A Compact Dielectric Large-Area Photon Detector". In: *Instruments* 2.1 (Feb. 2018), p. 3. ISSN: 2410-390X. DOI: 10.3390/instruments2010003. URL: http://www.mdpi.com/2410-390X/2/1/3.

[74] M. Auger et al. *ProtoDUNE-ND: proposal to place the ArgonCube 2x2 Demonstrator on-axis in NuMI*. Tech. rep. URL: https://docs.dunescience.org/cgi-bin/private/ShowDocument?docid=12571.

[75] J. Sinclair and C. Wilkinson. *ProtoDUNE-ND: proposal to place the ArgonCube 2x2 Demonstrator on-axis in NuMI*. DUNE document 12571-v1. DUNE, 2019.

[76] L. Aliaga et al. "Design, calibration, and performance of the MINERνA detector". In: *Nucl. Instrum. Meth.* A743 (2014), pp. 130–159. DOI: 10.1016/j.nima.2013.12.053. arXiv: 1305.5199 [physics.ins-det].

[77] P. Adamson et al. "The NuMI Neutrino Beam". In: *Nucl. Instrum. Meth.* A806 (2016), pp. 279–306. DOI: 10.1016/j.nima.2015.08.063. arXiv: 1507.06690 [physics.acc-ph].

[78] A. Machado and E. Segreto. "ARAPUCA a new device for liquid argon scintillation light detection". In: *Journal of Instrumentation* 11.02 (Feb. 2016), pp. C02004–C02004. ISSN: 1748-0221. DOI: 10.1088/1748-0221/11/02/C02004. URL: https://iopscience.iop.org/article/10.1088/1748-0221/11/02/C02004.

[79] C. Benson, G. D. O. Gann, and V. Gehman. "Measurements of the intrinsic quantum efficiency and absorption length of tetraphenyl butadiene thin films in the vacuum ultraviolet regime". In: *Eur. Phys. J. C* 78 (2018), p. 329. DOI: 10.1140/epjc/s10052-018-5807-z. URL: https://doi.org/10.1140/epjc/s10052-018-5807-z.

[80] EljenTechnology. *EJ-280, EJ-282, EJ-284, EJ-286 - Wavelength Shifting Plastics - Eljen Technology*. 2016. URL: https://eljentechnology.com/products/wavelength-shifting-plastics/ej-280-ej-282-ej-284-ej-286 (visited on 11/03/2020).

[81] B. E. Films, D. Brightness, and E. Films. *Vikuiti ™ Enhanced Specular Reflector (ESR) A relector for a brighter , more efficient display Features : 3 Innovation Vikuiti ™ Enhanced Specular Reflector (ESR)*. 2016.

[82] Hamamatsu. *Hamamatsu S13360-6050VE datasheet*. Tech. rep. URL: https://www.hamamatsu.com/resources/pdf/ssd/s13360-2050ve_etc_kapd1053e.pdf (visited on 11/05/2020).

[83] G. Di Domenico. 2011. URL: http://demonstrations.wolfram.com/FresnelEquations/ (visited on 01/13/2021).

[84] Cleateech LLC. *Cleatech LLC - Vacuum Desiccator Cabinets 1300 Series*. URL: https://www.cleatech.com/product-category/desiccators-dry-boxes/vacuum-desiccator-cabinets-1300/ (visited on 11/12/2020).

[85] D. Whittington, S. Mufson, and B. Howard. "Scintillation light from cosmic-ray muons in liquid argon". In: *Journal of Instrumentation* 11.5 (2016). ISSN: 17480221. DOI: 10.1088/1748-0221/11/05/P05016.

[86] L. Manenti. "Liquid Argon Time Projection Chambers for Dark Matter and Neutrino Experiments". PhD thesis. University College London, 2016. URL: https://discovery.ucl.ac.uk/id/eprint/1517934/.

Erklärung

gemäss Art. 30 RSL Phil.-nat. 18

Name/Vorname: Calivers Livio

Matrikelnummer: 14-916-795

Studiengang: Physik

Bachelor ☐ Master ☑ Dissertation ☐

Titel der Arbeit: Development and Characterisation of a Novel Light Detector: ArCLight

LeiterIn der Arbeit: Prof. Dr. Igor Kreslo

Ich erkläre hiermit, dass ich diese Arbeit selbständig verfasst und keine anderen als die angegebenen Quellen benutzt habe. Alle Stellen, die wörtlich oder sinngemäss aus Quellen entnommen wurden, habe ich als solche gekennzeichnet. Mir ist bekannt, dass andernfalls der Senat gemäss Artikel 36 Absatz 1 Buchstabe r des Gesetzes vom 5. September 1996 über die Universität zum Entzug des auf Grund dieser Arbeit verliehenen Titels berechtigt ist.
Für die Zwecke der Begutachtung und der Überprüfung der Einhaltung der Selbständigkeitserklärung bzw. der Reglemente betreffend Plagiate erteile ich der Universität Bern das Recht, die dazu erforderlichen Personendaten zu bearbeiten und Nutzungshandlungen vorzunehmen, insbesondere die schriftliche Arbeit zu vervielfältigen und dauerhaft in einer Datenbank zu speichern sowie diese zur Überprüfung von Arbeiten Dritter zu verwenden oder hierzu zur Verfügung zu stellen.

Bern, 07.01.2020

Ort/Datum

Unterschrift